Equilibrium Analysis and Control of a Non-neutral Plasma in a Toroidal Magnetic Shear Configuration

A Thesis submitted to
the Graduate School of Frontier Sciences, University of Tokyo
in partial fulfillment of the requirements for the degree of
Master of Science in Advanced Energy

Directed by Professor Yoshida Zensho

Saitoh Haruhiko
saito@plasma.q.t.u-tokyo.ac.jp

Department of Advanced Energy
Graduate School of Frontier Sciences
University of Tokyo

7-3-1 Hongo, Bunkyo-ku, Tokyo 113-0033 Japan

February 2002

Abstract

The conventional rigid rotation model of thermal equilibrium does not apply to a toroidal non-neutral plasma trap; the non-uniformity of the magnetic field produces an inhomogeneous flow. For sufficiently large ω_c/ω_p (ω_c: cyclotron frequency, ω_p: plasma frequency), the flow can be approximated by the $\mathbf{E} \times \mathbf{B}$ drift velocity. The toroidal equilibrium of an electron plasma has been analyzed for a rather complex geometry of magnetic shear configuration.

The potential structures of a toroidal non-neutral plasma were measured by an emissive probe array. The obtained potential profiles show that the injected electrons diffuse from the beam orbit and spread toward the confinement region of the torus. Although the shape of the potential profile did not agree with the numerical analysis, the ”paramagnetism” of a non-neutral plasma, predicted by the $\mathbf{E} \times \mathbf{B}$ drift model, was observed. The disagreement was possibly due to the perturbation by support rods and the beam component of the plasma.

Aiming for an active control of a plasma, a pair of plasma control electrodes were installed in Proto-RT. The external electric fields generated by the electrodes penetrated into the plasma, and the alteration of both potential and density profiles were observed.

Acknowledgments

I am most grateful to Professor Yoshida Zensho. He gave me very interesting subjects in both numerical analisys and experiments, and patiently guided me in spite of my slow progress. His accurate and positive advice always helped me and encouraged me. I could never have completed this thesis without his instruction.

I also appreciate Professor Himura Haruhiko, Professor Fukao Masayuki, Mr. Morikawa Junji, Dr. Nakashima Chihiro, Dr. Kondoh Shigeo, and Mr. Yagi Keita for their instruction especially in the experiments. They guided me in all about the practical experimental technique in Proto-RT, from its operation method to the circuit construction.

I also express my deepest gratitude to Professor Ogawa Yuichi for his instruction and encouragement. His suggestive advice helped me in the equilibrium analysis.

In the calculation of equilibrium, I am indebted to Mr. Ohsaki Shuichi, Dr. Ito Atsushi, Dr. Tatsuno Tomoya, and Mr. Numata Ryusuke for their instruction.

This study has never been carried out without the help of the members of the laboratory. I am grateful to all the members for their encouragement and instructive discussion in the seminars.

I am also grateful to Professor Terumichi Yasushi, Professor Maekawa Takashi, Professor Tanaka Hitoshi, and Dr. Asakawa Makoto for their direction during my days of an undergraduate student in Kyoto University. It was very valuable experience that I could carry out the experiments in basic devices of plasma confinement under their instruction.

Finally, I would like to thank my family for their concern and support.

Saitoh Haruhiko

Contents

List of Figures

Chapter 1

Introduction

There is an increasing interest in diverse applications of non-neutral plasmas; traps of charged particles (including anti-matters)[1] play an essential role in nuclear and atomic physics experiments, as well as in many different applications such as medical and material diagnostics. The self-electric field and the resultant strong flow are also applied to the study of both nonlinear vortex dynamics and various types of structure formations. Recently, the self-organization of a strong diamagnetic (high-beta) state was predicted by a two-fluid model.[2,3] Studies on these non-neutral (or strong flow) systems may open up an innovative path toward the advanced fusion concept.

Toroidal systems have advantages in trapping high energy, high density charged particles, or multiple species of different charges, because they do not use external electric fields to plug open magnetic field lines.[4–8] The Proto-RT (Proto-type Ring Trap) device, shown in Figs. 1.1 and 3.1, was constructed to study various physical phenomena in toroidal non-neutral plasmas.[9] Proto-RT can operate with a variety of magnetic field configurations, which are generated by two kinds of poloidal field coils (an internal conductor coil and two vertical field coils) in addition to toroidal field coils. This system enables us to test innovative concepts, such as particle injection across magnetic surfaces[11,12] and plasma stabilization by the effect of magnetic shear.[13]

In Proto-RT, electrons are injected by an electron gun placed near the magnetic separatrix. In the peripheral region, electrons trace chaotic orbits, and strong randomization causes effective spreading of the beam. Because of the long orbits of chaotic motion, non-adiabatic effects yield diffusion toward the confinement region.[9] Thermalized electrons generate a macroscopic equilibrium. In this paper, we study the structure of the non-neutral plasma equilibrium and its control method in a toroidal device of the Proto-RT type (i.e, toroidal magnetic shear-internal conductor system).

In Chapter 2, the equilibrium will be numerically analyzed by the $\mathbf{E} \times \mathbf{B}$ drift model. The plasma showed paramagnetism being confined to the strong magnetic field side of the torus. The equilibrium was also controlled by externally applied electric fields, as well as by the magnetic field configurations. The effect of the external electric fields on the equilibrium was studied, and accordingly, new control method of a toroidal non-neutral plasma was proposed.

Two-dimensional potential profiles of a toroidal non-neutral plasma were measured by an emis-

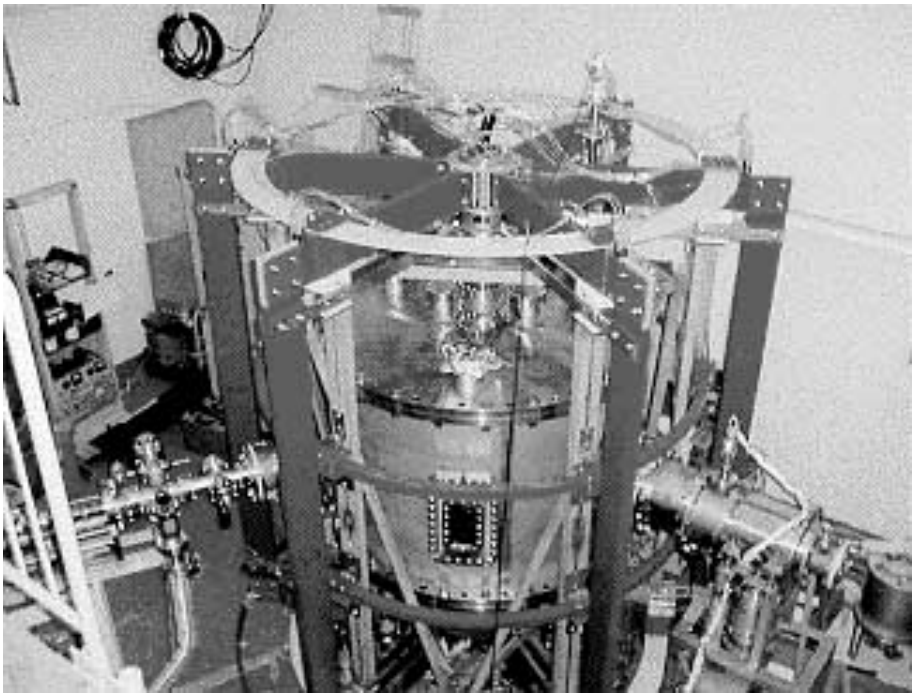

Figure 1.1: Photographic view of the Proto-RT device

sive probe array in Proto-RT (Chapter 4). Although the obtained potential structure is quite different from the calculated results, they showed rather similar tendency to the numerical calculation, especially in the magnetic field strength-dependence. The difference is supposed to be caused by the effect of the diffusion toward the device vessel, unmagnetized beam component of the electron plasma, and the disturbance by the supporting rods of the internal conductor in Proto-RT. Based on the calculation in Chapter 2, a pair of plasma control electrodes were designed and installed in Proto-RT. The effects of external electric fields will also be discussed in this Chapter.

Chapter 2

Equilibrium Analysis

2.1 The E × B equilibrium model and the calculation method

For a low density magnetized non-neutral plasma, we can use the $\mathbf{E}\times\mathbf{B}$ approximation of the flow velocity;[4]

$$\mathbf{v} = -\frac{\nabla\phi\times\mathbf{B}}{B^2}, \tag{2.1}$$

where ϕ is the electrostatic potential. In the equation of motion as a fluid plasma:

$$mn\left[\frac{\partial v}{\partial t} + (\mathbf{v}\cdot\nabla)\mathbf{v}\right] = nq(\mathbf{E}+\mathbf{v}\times\mathbf{B}) - \nabla\cdot\mathbf{P}, \tag{2.2}$$

the ratio of the convection term to the electric and magnetic force is given by $q \equiv {\omega_p}^2/{\omega_c}^2$ (ω_p: plasma frequency, ω_c: cyclotron frequency). Here we assumed the fluid element motion of the $\mathbf{E}\times\mathbf{B}$ drift speed $v_E = E/B$, and used the Debye length λ_D as a typical length of the plasma. In the experiments of low density plasmas, $q \ll 1$ (For an electron plasma of $n = 10^{13}\ m^{-3}$ and $B = 10^{-2}\ T$, $q = 10^{-2}$) and the convection term is almost negligible. In a cold plasma, the pressure term $\mathbf{P}$ is also negligible, and the $\mathbf{E}\times\mathbf{B}$ drift approximation is applicable.

In the limit of $q \to 0$, this kind of guiding center motion coincides with the particle motion. Then the charged particle moves along an equipotential contour: $\nabla\phi\cdot\mathbf{v} = 0$. Using the $\mathbf{E}\times\mathbf{B}$ speed and this equation, the continuity equation in a steady state reads

$$\nabla\cdot(n\mathbf{v}) = -\left[\nabla\phi\times\nabla\left(\frac{n}{B^2}\right)\right]\cdot\mathbf{B} = 0. \tag{2.3}$$

Here, n is the number density of charged particles. When the magnetic field $\mathbf{B}$ has a component perpendicular to $\nabla\phi$, (2.3) demands

$$\nabla\phi\times\nabla\left(\frac{n}{B^2}\right) = 0. \tag{2.4}$$

This condition applies for an axisymmetric toroidal device with a toroidal magnetic field. Equation (2.4) implies that

$$n = B^2 f(\phi), \tag{2.5}$$

where f is a certain smooth function of ϕ.

The n and ϕ must also satisfy the Poisson equation

$$\nabla^2\phi = -\frac{qn}{\varepsilon_0} \tag{2.6}$$

with boundary conditions (q is the charge, ε_0 is the vacuum dielectric constant). We can replace the boundary condition by the corresponding image charge ρ_i induced on the conductor walls. The total charge in the system is given by $\rho = qn + \rho_i$. We decompose $\phi = \phi_p + \phi_i$ imposing

$$\nabla^2\phi_p = -\frac{qn}{\varepsilon_0} = -\frac{qB^2}{\varepsilon_0} f(\phi), \tag{2.7}$$

$$\nabla^2\phi_i = -\frac{\rho_i}{\varepsilon_0}, \tag{2.8}$$

with the homogenized boundary condition $\phi_p|_\infty = \phi_i|_\infty = 0$.

Equation (2.7) is integrated as

$$\phi_p(\mathbf{r}) = \frac{q}{4\pi\varepsilon_0}\int_{-\infty}^{\infty} \frac{B^2 f(\phi)}{|\mathbf{r}-\mathbf{r}'|} d\mathbf{r}'. \tag{2.9}$$

For an axisymmetric toroidal plasma, (2.9) reads in the cylindrical coordinate (r,θ,z),

$$\begin{aligned}\phi_p(\mathbf{r}) &= -\frac{e}{4\pi\varepsilon_0}\iiint \frac{B(\mathbf{r}')^2 f(\phi(\mathbf{r}'))r'dr'd\theta'dz'}{r^2+r'^2+(z-z')^2-2rr'cos\theta'} \\ &= \frac{e}{4\pi\varepsilon_0}\iint B(\mathbf{r}')^2 f(\phi(\mathbf{r}'))A(\mathbf{r},\mathbf{r}')dr'dz'. \end{aligned} \tag{2.10}$$

The kernel $A(\mathbf{r},\mathbf{r}')$ is defined by

$$A(\mathbf{r},\mathbf{r}') = \frac{k}{2}\sqrt{\frac{r'}{r}}K(k),$$

where $K(k)$ is the complete elliptic integral of the first kind:

$$K(k) = \frac{k^2}{2}\int_0^{\frac{\pi}{2}} \frac{d\theta}{\sqrt{1-k^2 sin^2\theta}},$$

$$k^2 = \frac{4rr'}{(r+r')^2+(z-z')^2}.$$

For the image charge, we integrate (2.8) in a similar form:

$$\phi_i(\mathbf{r}) = \frac{1}{4\pi\varepsilon_0}\int_{-\infty}^{\infty} \frac{\rho_i(\mathbf{r}')}{|\mathbf{r}-\mathbf{r}'|} d\mathbf{r}'. \tag{2.11}$$

The image charge ρ_i and the corresponding potential ϕ_i are determined by the boundary condition. When the wall conductors are grounded, for example, we impose

$$\phi = \phi_p + \phi_i = 0 \tag{2.12}$$

on the boundary. In the calculations, we use delta-measure image charges distributed on the conducting walls (Fig. 2.1). The boundary condition is examined at the same number of points on the conductors, and the image charges are adjusted to satisfy (2.12).

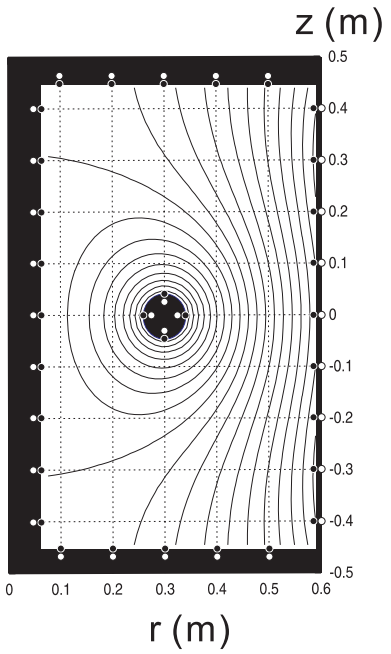

Figure 2.1: Delta-measure image charges used in calculations, on the poloidal cross section of Proto-RT. The ring electric charges (○) are iteratively calculated, so that boundary conditions are satisfied on the conductor's surface (●).

2.2 Structure of a toroidal non-neutral plasma equilibrium

The method given in the previous section is applicable to rather complex magnetic field configurations and vessel shapes.[14] We consider an electron plasma in a toroidal device in which a dipole magnetic field is generated by an internal conductor. Combining vertical and toroidal fields, a variety of magnetic field configurations can be created. In this section, the structure of an electron plasma and its control methods in such configurations are discussed.

2.2.1 Paramagnetic equilibrium of a toroidal non-neutral plasma

In the present $\mathbf{E} \times \mathbf{B}$ drift model of equilibrium, the plasma density concentrates in a preferential high-magnetic field region (a kind of paramagnetism). Hence, the plasma shifts inward in a toroidal device. The particle injection method of Proto-RT arranges a particle source in a weak-field place. The confinement region and the particle source can be naturally separated.

When a magnetized electron moves with an $\mathbf{E} \times \mathbf{B}$ drift speed that is inversely proportional to the magnetic field strength B, the electron spends a longer time in a region of larger B. Hence, the plasma shows "paramagnetism". When a toroidal magnetic field is applied, and consequently the velocity of an electron has a poloidal component, electron distribution will shift inward, because the toroidal field has a $1/r$ profile (r: radius from the axis of the torus). Superposition of poloidal

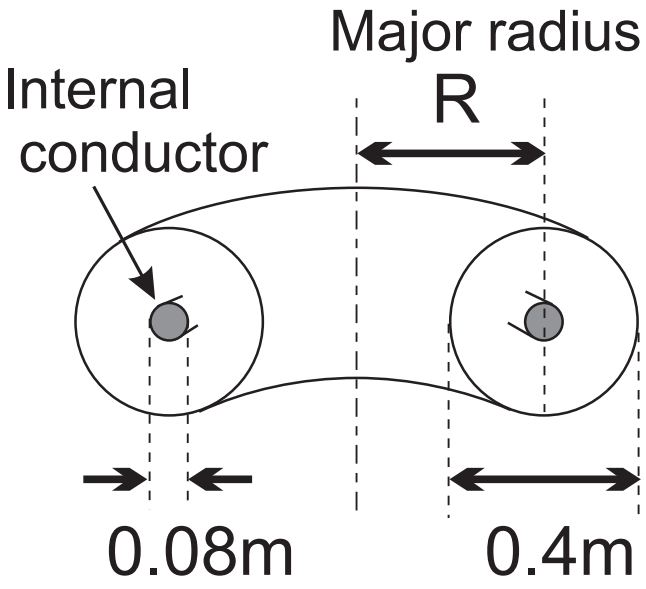

Figure 2.2: Simple model of toroidal internal conductor device. Changing the major radius R, we examine the toroidal effect (Figs. 2.3 and 2.4).

fields modifies the field distribution and hence modifies the density profile.

To overview the basic property of equilibrium, we have studied solutions in circular domains of a poloidal cross-section with some different aspect ratios (Fig. 2.2). Figure 2.3 shows the potential profiles when the magnetic field is generated mainly by an internal conductor. The function f in (2.5) is assumed to be a linear function of the potential ϕ. For typical number density of the plasma $n = 10^{11}m^{-3}$, typical electron temperature $T_e = 10eV$, and typical magnetic field strength $B = 10^{-2}T$, $\omega_c/\omega_p \sim 10^2$ and $L/\lambda_D \sim 10^1$ (L: typical length of the plasma, λ_D: Debye length). When the aspect ratio of the device is large, the magnetic field is approximately uniform, and the potential profile becomes almost symmetric in the r-z plane. In this case, electrons describe helical drift orbits circulating around the internal conductor with almost constant velocity. For a small aspect ratio, the non-uniformity of the magnetic field becomes strong, and the plasma shifts inward due to the paramagnetism.

The other reason why the equilibrium density shifts inward is the effect of image charges on the boundary.[15] The electric field in a toroidal plasma arises both from its space charges and also from the image charges on electrical conductors. Macroscopically, the equilibrium of a toroidal non-neutral plasma is understood as the force balance of two forces; one is the ”hoop force” and the other is the force due to the induced image charges on the conductors.

The hoop force of a non-neutral plasma is a repulsive force due to the charges of a single species. Approximated from Poisson’s equation, a large aspect ratio (i.e, $a/R \ll 1$) toroidal non-

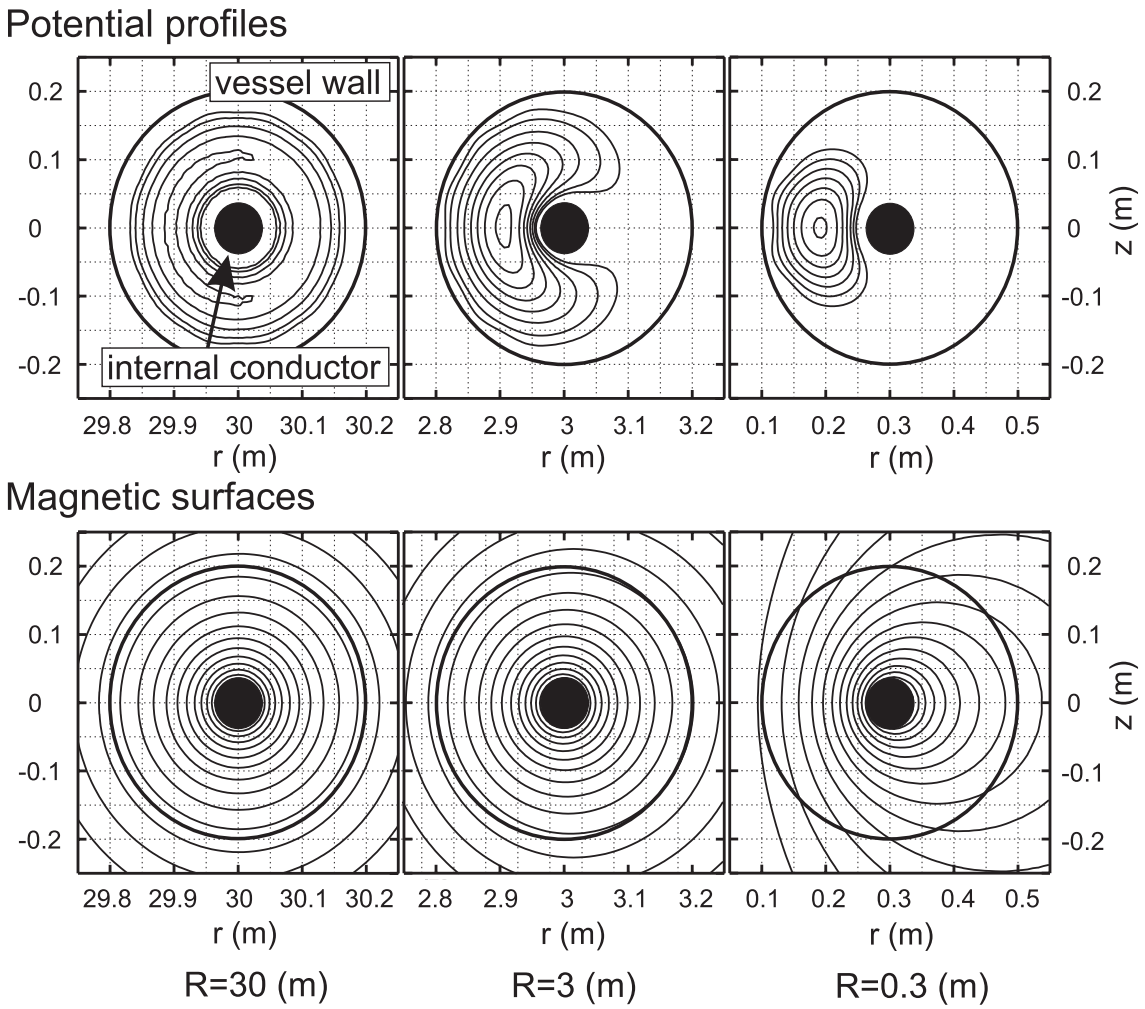

Figure 2.3: Potential profiles and magnetic surfaces in a poloidal cross-section of toroidal devices with different major radii (See Fig. 2.2). Electrostatic potentials on both the boundaries of vessel walls and the internal conductor are assumed to be zero. The magnetic field was mainly generated by the internal conductor, and weak toroidal magnetic field is also applied.

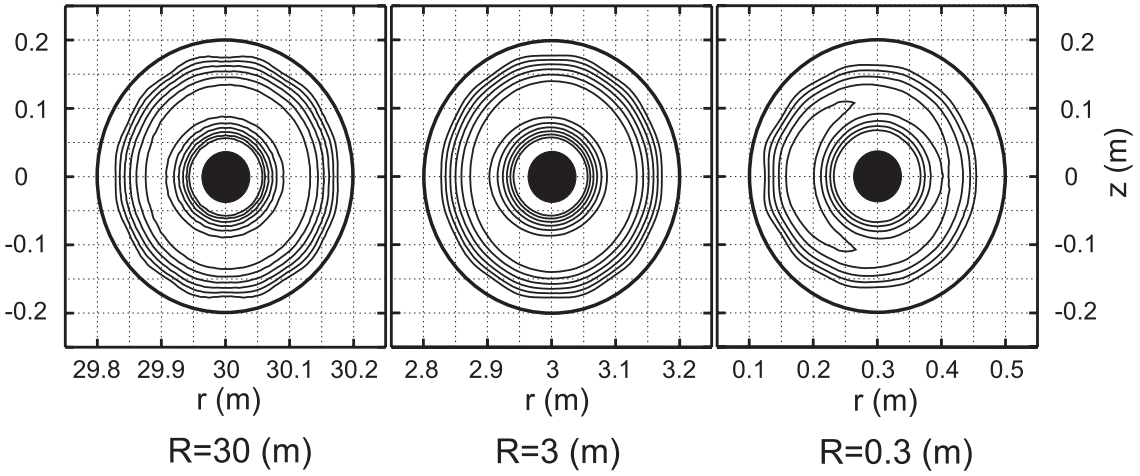

Figure 2.4: Potential profiles in artificial homogeneous magnetic fields. The other conditions, except for the magnetic field strength, are the same as those in Fig. 2.3.

neutral plasma has a capacitance C of

$$C \simeq \frac{4\pi^2 \varepsilon_0 R}{ln\big(R/a\big)}. \tag{2.13}$$

Using this capacitance C, the electrostatic hoop force F_H is given by

$$F_H \simeq -\frac{1}{2}\Phi^2 \frac{dC}{dR}, \tag{2.14}$$

where Φ is the typical potential in the plasma. Even if no external electric field is applied, this hoop force F_H can be balanced by the forces from image charges on chamber conductors. When the plasma is radially shifted in a toroidal device, and the distribution of image charges is also uneven, the plasma feels a net force along the $+\mathbf{r}$ direction. In Fig. 2.4, we assume an artificial homogeneous magnetic field strength in order to examine this effect. The toroidal curvature proceeds as a hoop force. When the plasma shifts inward, this force can be cancelled by an electrostatic drag force generated by the image charges on the conductors.

2.2.2 Position and shape control in Proto-RT

One of the advantages of a toroidal internal-conductor trap stems from its high degree of freedom to control the plasma. By changing magnetic field and boundary potentials, we can produce a variety of equilibria.

The position and shape of the toroidal plasma equilibrium can be controlled by changing the magnetic field and also by applying external electric fields with changing the boundary potentials. We tested these effects in the geometry of Proto-RT. Figure 2.5 shows equilibria in three different

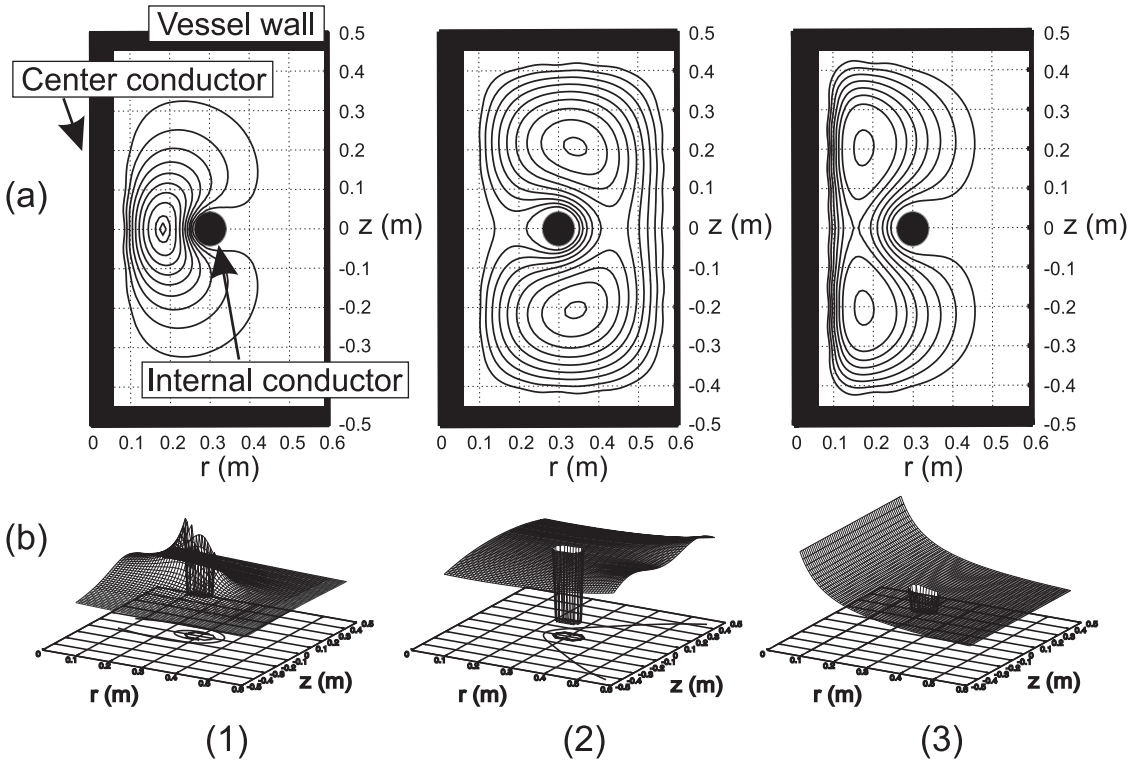

Figure 2.5: Control of equilibrium by magnetic field. (a) Potential profiles in the Proto-RT device. (b) Profiles of the magnetic field strength. (1) dipole magnetic field plus toroidal field, (2) vertical field plus toroidal field, and (3) only toroidal field.

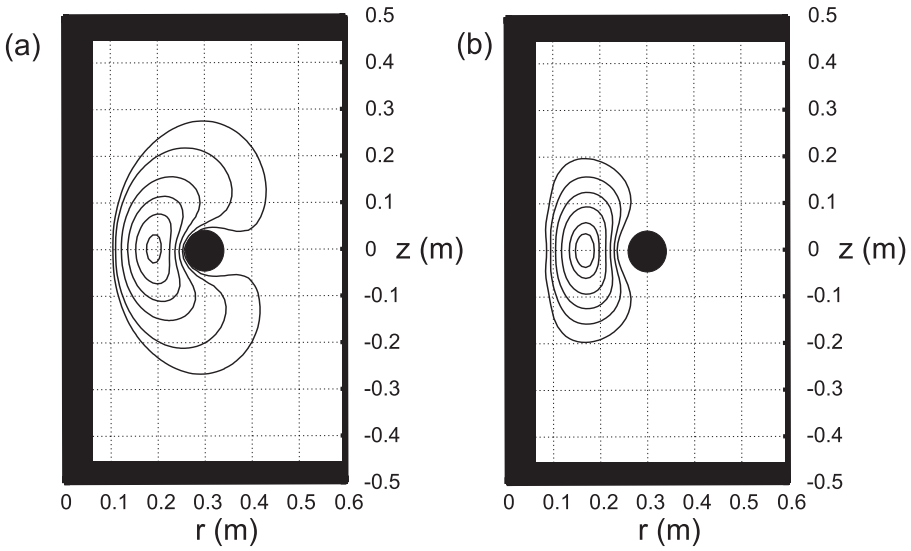

Figure 2.6: Control of equilibrium by external electric field. The applied potentials on the center conductors are (a) $+\phi_{max}/10$ and (b) $-\phi_{max}/10$, where ϕ_{max} is the maximum potential inside the plasma. The magnetic field is same as that in Fig. 2.5.(1).

types of magnetic fields. The potential profiles show paramagnetism, as mentioned in the previous subsection, while the structures are more complicated because of realistic field configurations and the device geometry of the Proto-RT device. (The function f of (2.5) and plasma parameters are the same as in the previous calculations.) We observe the strong influence of the image charges on the internal conductor. The image charges, having the opposite sign of the plasma charge, diminish the space potential near the conductor. If the magnetic field is not strong enough on the equatorial plane of the device, the profile of plasma separates into two peaks. Because the guiding center of particles parallels the level sets of the potential, the particles are divided into two groups.

The boundary condition of the potential can be changed by biasing the internal conductor and/or a certain part of the vessel. This degree of freedom provides us the other parameters necessary to control the equilibrium. In Fig. 2.6, we observe that the equilibrium is strongly influenced by a relatively small change of the boundary potentials (1/10 of the maximum potential of the plasma). This method may be useful in optimizing the stability and confinement of the plasma.

2.3 The effects of image charges on equilibrium

As discussed in subsection 2.1, in this equilibrium analysis, the image charge on the surrounding conductors are introduced, instead of an free boundary condition. The effects of image charges on the density of toroidal non-neutral plasma were analyzed. In toroidal devices, the external fields generated by image charges will repress repulsive electric forces between space charges. This effect is supposed to be advantageous to the high density confinement of a non-neutral plasma.

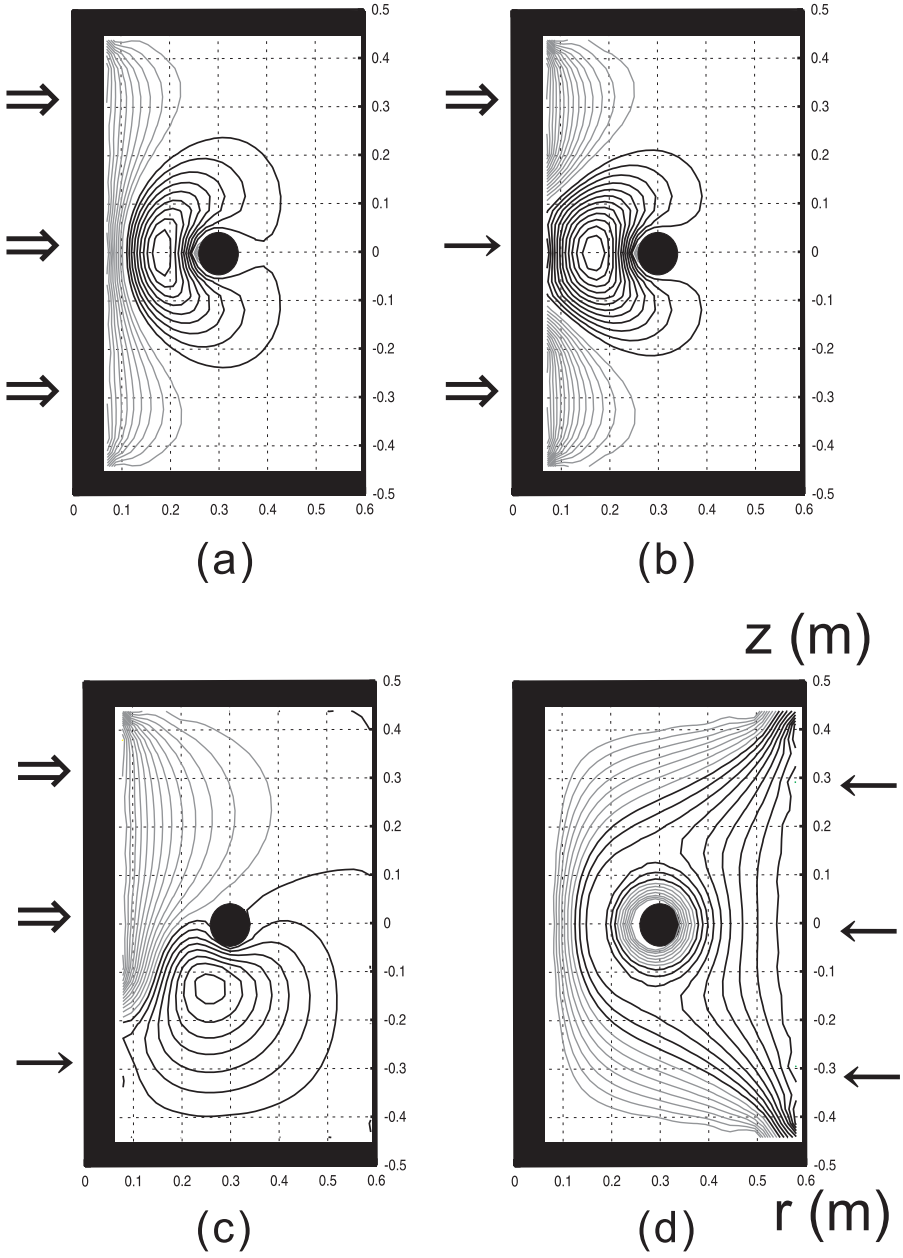

Figure 2.7: The variation of plasma control by the external electric field. The same sign (narrow arrow) and the opposite sign (bold arrow) of external potential is applied on the vessel wall.

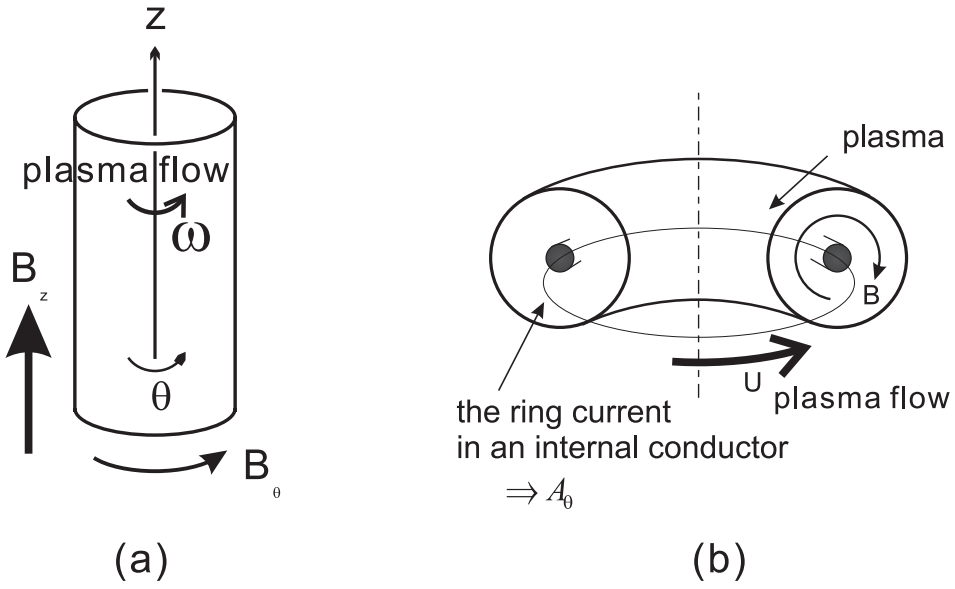

Figure 2.8: Cylindrical and simple toroidal device.

2.3.1 Brillouin density limit in the thermal equilibrium

An infinitely-long equidensity cylindrical plasma, described in Fig. 2.8 (a), is confined by a balance between the outward Coulomb and centrifugal forces and the inward Lorentz force:

$$-\frac{m{v_\theta}^2}{r} = -qE_r - qv_\theta B_z, \tag{2.15}$$

where $E_r = qnr/2\varepsilon_0$ is in the radial electric field generated by space charges. In thermal equilibrium of rigid rotation: $v_\theta = r\omega$, the force balance equation is reduced to the Brillouin density limit:[16]

$$-\frac{2{\omega_p}^2}{{\omega_c}^2} \leq 1, \tag{2.16}$$

where ${\omega_p}^2 = ne^2/\varepsilon_0 m$ is the plasma frequency, $\omega_c = eB/m$ is the cyclotron frequency. When external electric fields are applied, the thermal equilibrium is not formed (e.g, the external field by an axisymmetric electrode is given by $a_0 + a_1 r^2 + a_2 logr$).

For a toroidal non-neutral plasma in only poloidal fields (Fig. 2.8 (b)), it was also shown that the density of confined particle in the thermal equilibrium is always equal to or less than usual Brillouin density limit.[17, 18]

2.3.2 Numerical calculation in Proto-RT

In a magnetic configuration of both toroidal and poloidal fields, the effect of image charges on potential profiles were calculated. The potential in a plasma ϕ is the sum of ϕ_{plasma}: the potential

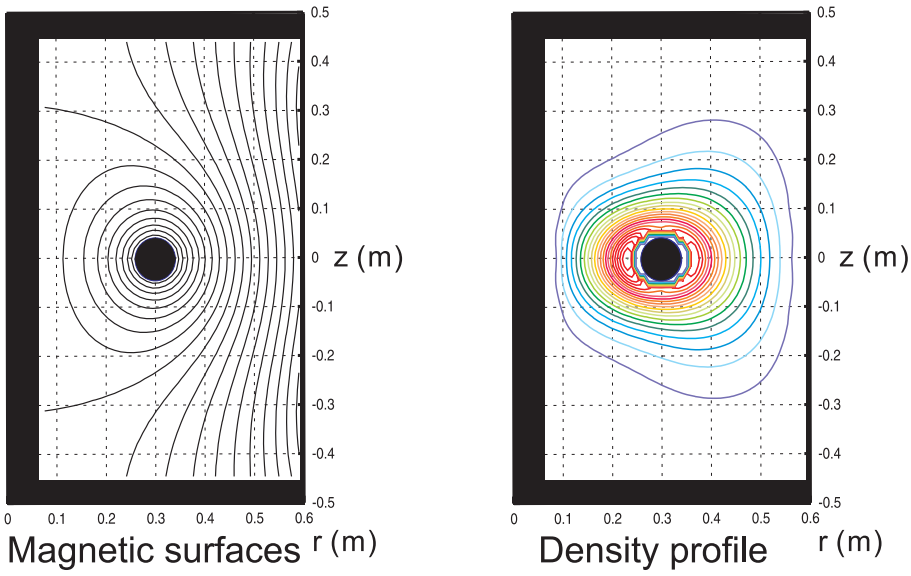

Figure 2.9: The assumed magnetic surface and the density profile in Proto-RT. Potential profiles were calculated (Fig. 2.10) for this configuration of toroidal non-neutral plasma.

generated by space charges, and ϕ_{image}: the potential generated by image charges on conductors (e.g, vessel walls). In an infinitely long and symmetric linear device, ϕ_{image} in the plasma is equal to 0, but in a toroidal device, the image charges will generate finite electric fields inside the torus. As the opposite sign of charges are induced on conductors, it leads to the depression of potential in the plasma. Especially in toroidal-internal conductor devices, like Proto-RT, this effect is quite large, because the internal conductor is located inside the plasma. The potential profile calculated from the the density profile in Fig. 2.9 is shown in Fig. 2.10. Due to the image charges (b) on the torus chamber and also (c) on the internal conductor, the net potential was reduced to 10percent of the potential generated by the space charge. When the conductors in the vessel are properly biased, the effects of potential depression in the plasma became large. Because the repulsive electric fields between the particles are reduced, it may contribute to the improvement of the plasma property.

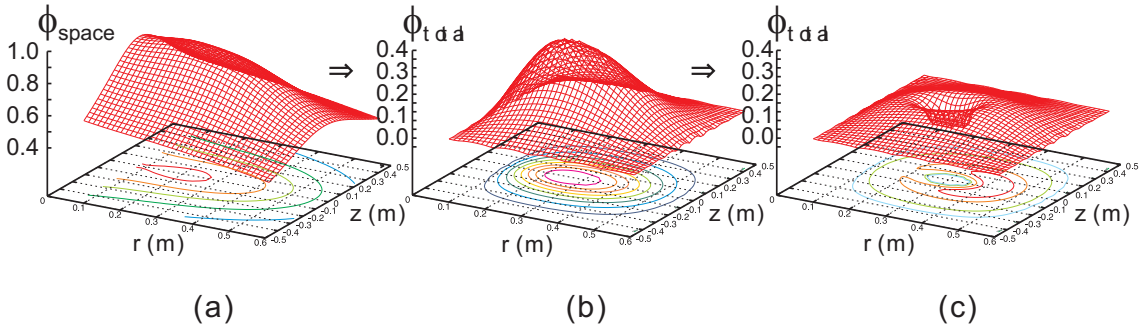

Figure 2.10: Potential repression in toroidal devices. Potential profiles are calculated (a) in a vacuum space, without the image charges, (b) in a simple toroidal device, and (c) in a toroidal-interal ring device. The potential is normalized by the peak value of (a).

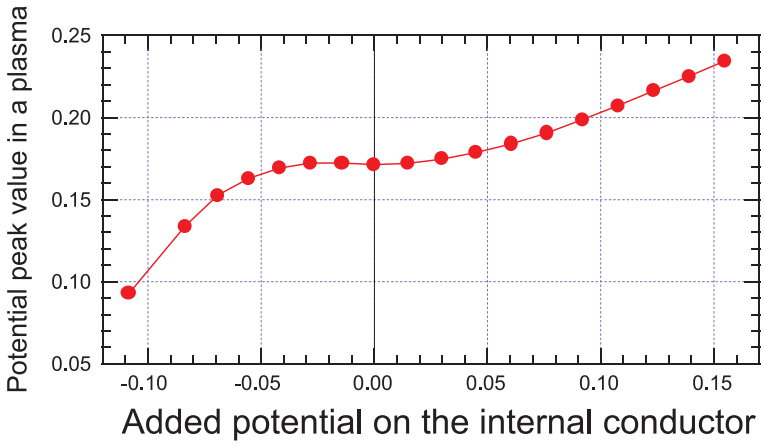

Figure 2.11: Plasma control by the external electric field. The same sign (narrow arrow) and the opposite sign (bold arrow) of external potential is applied on the vessel wall.

Chapter 3

Experimental Setup and Diagnostics

The goal of this work is to understand and to control the equilibrium of a toroidal non-neutral plasma. Aiming for an active control method of a plasma, a pair of plasma control electrodes were installed in the Proto-RT device. An emissive Langmuir probe array was constructed for the measurements of space potential structures. The diagnostics of emissive probes will be discussed together with experimental considerations.

3.1 The Experimental Setups

All experiments were carried out at Proto-RT (Prototype-Ring Trap),[9,10] a toroidal non-neutral plasma trap. General descriptions of the devices are given.

3.1.1 Proto-RT

A schematic view and parameters of the Proto-RT device is given in Fig. 3.1 and Table. 3.1. The torus has a rectangular poloidal cross section of $0.9\ m \times 0.472\ m$, and the toroidal fild (TF) coils are penetrating through its hollow center stack of $0.114\ m$ diameter. Besides the TF coils, Proto-RT has two kinds of poloidal field coils; an internal conductor (IC) coil for the dipole field and a pair of vertical field (VF) coils. The IC coil is suspended in the chamber by eight support rods, which are stuck to the center stack. The major radius of the IC coil is $0.3\ m$. The VF coils are located at outside of the chamber with a vertical interval of $0.6\ m$. Its diameter is $0.9\ m$, and almost straight magnetic lines of force are obtained inside the chamber. Each coil current is fed by a DC power source of $50\ V, 500\ A$ (TF), $60\ V, 60\ A$ (IC), and $120\ V, 30\ A$ (VF). In this study, IC and TF coils were used. The typical strength of the magnetic field was $10^{-2}\ T$.

Electrons are injected by an electron gun of LaB_6 cathode located at $z = 0$ plane. The gun is movable along the radial direction and the angle of electron injection can also be freely aligned. The emission current at $2\ kV$ bias and no magnetic field was $750\ mA$. In this study, the gun was located at $r = 0.465\ m$ and the injection angle was decided according to the numerical calculation of the particle orbit.

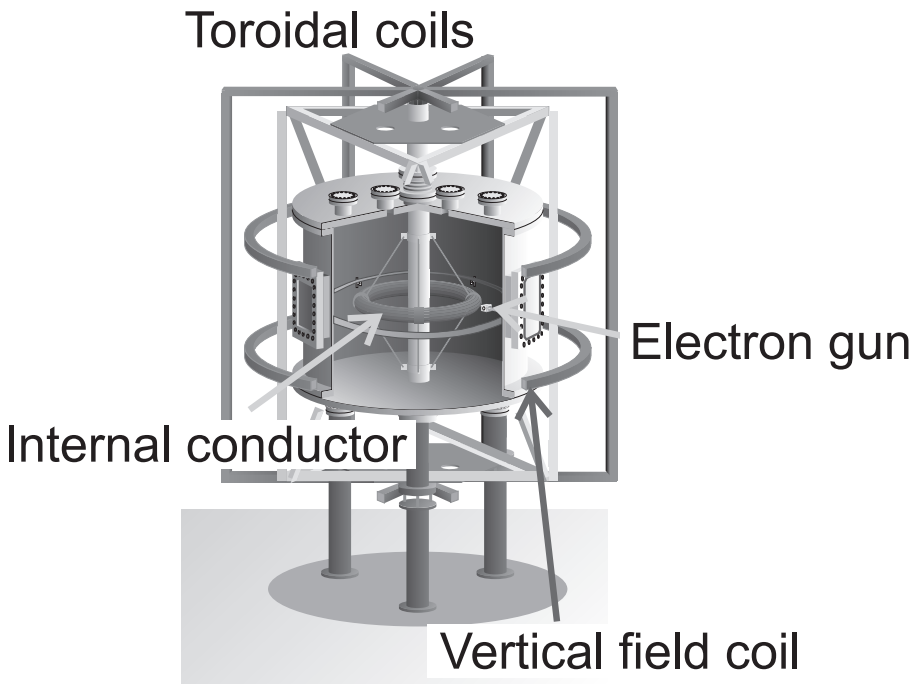

Figure 3.1: Proto-RT, a schematic view. A toroidal non-neutral plasma confinement device, capable of generating various kinds of magnetic field configurations.

The chamber is drew to a base pressure of 3×10^{-7} *Torr* by a turbomolecular pump. Two mechanical rotary pumps are also equipped, one for roughing from the atmospheric pressure and another for differential evacuation near the rotating flange of the electron gun.

Proto-RT has three maintenance ports (41 $cm \times 26$ *cm*, sealed with O-rings) on the side face and twelve diagnostic ports (ICF152) on the top and bottom faces of the vessel. Several diagnostic ports are used for the power supply cable and the cooling tubes of the IC coils. The diagnostic flange, attached to one of the maintenance ports, has twenty-two gauge ports (ϕ 0.7) from $z = -20$ *cm* to 20 *cm* at vertical intervals of 2 *cm*.

3.1.2 Plasma control electrodes

As discussed in Sec. 2.2.2, the equilibrium of a non-neutral plasma is influenced by external electric fields from outside of the space charges. As far as an equilibrium is found, this external fields are automatically generated by the induced image charges on the chamber. However, more actively, the equilibrium can be controlled by externally applied electric fields generated by electrodes. In this study, two plasma control electrodes were installed and its effects on the plasma was examined.

The center stack and the IC coil's jacket are both shorted to the ground (to the chamber of Proto-RT). Because it is difficult to separate them each other electrically, we have set insulating materials

Vacuum Vessel	Inner diameter	1.18 m
	Center stack diameter	0.114 m
	Height	0.9 m
	Base pressure	3×10^{-7} $Torr$
Internal Conductor (IC) Coil	Major radius	0.3 m
	Minor radius	0.043 m
	Coil current	10.5 kAT
	Cooling method	Freon
Vertical Field (VF) Coils	Major radius	0.9 m
	Coil current	5.25 kAT
	Cooling method	Air
Toroidal Field (TR) Coils	Coil current	30 kAT
	Cooling method	Water
Electron Gun	Cathode	LaB_6
	Acceleration voltage	2 kV
	Emision current ($B = 0$)	750 mA

Table 3.1: Parameters of Proto-RT

Internal Conductor (IC) Electrode	Major radius	0.3 m
	Minor radius	0.05 m
Center Stack (CS) Electrode	Major radius	0.09 m
	Height	0.6 m
Common Properties	Material	SUS304
	Thickness	1.0 mm
	Electrical insulation	more than 2 kV

Table 3.2: Parameters of plasma control electrodes

on the center stack and the jacket, and then installed the electrodes upon them. Each electrode is made of 1 *mm* thick SUS304 stainless steel. The parameters: Table 3.2, the configuration: Fig. 3.2, and the pictures: Figs. 3.4 and 3.5 of the electrodes are shown. Potential profiles generated by the electrodes in a vacuum (no plasma) chamber of Proto-RT are described in Fig. 3.3. The insulation of the electrodes was tested by a 1 kV 2000 $M\Omega$ high voltage tester and by a 2 kV power source for two minutes. The test was done between the chamber and each electrode, and, between each electrode in the atmospheric pressure.

The IC electrode was assembled from eight crescentic parts of 90° cut. The diameter of the electrode torus is 10 *cm*, and this is 1.5 *cm* larger than the IC coil jacket. The jacket is insulated by using of four pieces of teflon molding and kapton sheets. On the insulating material, the electrode is bound by $\phi 0.2$ stainless wire. The gap of each part was covered with a 50 μm thick stainless sheets, in order to repress the distortion of electric fields, and to hide the teflon molding from plasmas. Electrical connection of each part was also done by these sheets.

As a feeder, junfreon (teflon coated) wire was spot welded to the electrode near the coolant nozzle, and laid inside the nozzle insulator, then along the center stack, inside the CS electrode.

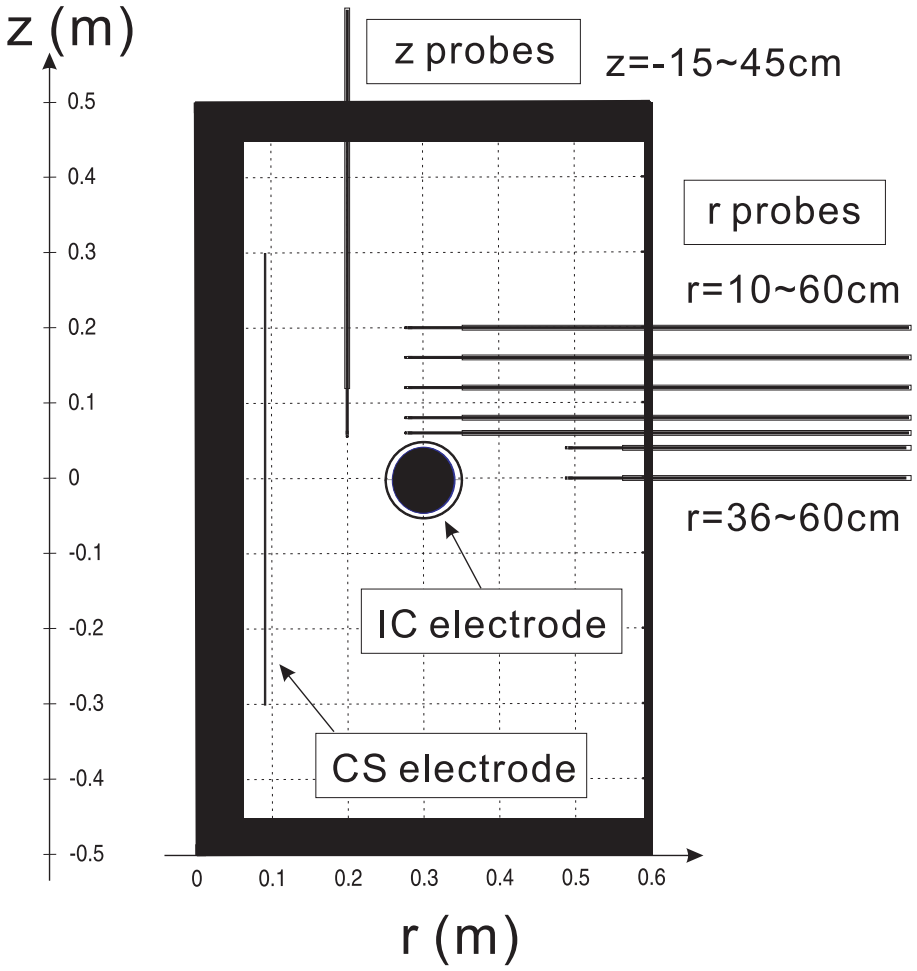

Figure 3.2: Configuration of electrodes and emissive probe array in the poloidal cross section of Proto-RT. Probes are located at $z = 0, 4, 6, 8, 12, 16, 20$ *cm* and $r = 20$ *cm*.

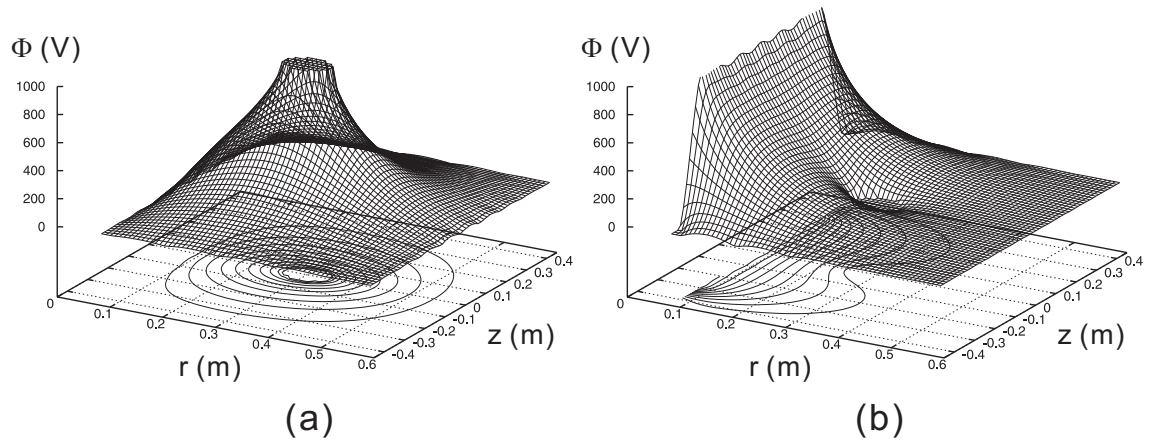

Figure 3.3: The vacuum (no plasma) potential profiles generated by plasma control electrodes on a poloidal cross section (cf. Fig. 3.2) of Proto-RT. A potential of 1 *kV* is applied to (a) the IC and (b) the CS electrode. The rest part of the chamber is shorted to the ground. The contours are plotted at intervals of 100 *V*.

The wire was covered by grounded stainless tubes for electric shield, and the exposed part of the wire was also covered by an alumina (SSA) insulating tube. The other end of the wire was connected to a power source via a ICF152 flange with electric terminals, at $r = 0.2$ *m* diagnostic ports on the bottom face of Proto-RT.

The CS electrode was installed for the generation of electric fields of the radial direction. To avoid the interference with the coolant nozzle and feeder cables, there is a space of 3 *cm* between the electrode and the center stack. The electrode is fixed to a pair of photoveel (ceramic) insulator, which is attached to the center stack. The diameter and height of the electrode is 18 *cm* and 60 *cm* each. The longitudinal length of 60 *cm* is limited by the support rods of the IC coil. However, the electric field in the confinement region (around $z = -20 \sim +20cm$) is almost smooth (Fig. 3.3 (b)) and the effects of the irregular field are supposed to be minimum. The way of electric connection to a power source and wiring is similar to that used for the IC conductor.

3.1.3 Probe construction and configuration

Schematic and photographic views of emissive Langmuir probe configuration are shown in Figs. 3.2 and 3.7. The probes were inserted from seven gauge ports (*r-probes*) on the diagnostic flange and one gauge port (*z-probe*) on a diagnostic port. The probes are manually movable along **r** (*r-probe*) or **z** (*z-probe*) direction, and we can obtain two-dimensional potential profiles.

The construction of the probe is given in Fig. 3.6. The probe tip was a thoria-tungsten (0.1 *mm* in diameter and approximately 10 *mm* long: surface area $S \simeq 3 \times 10^{-6}\ m^2$) filament and spot welded to molybdenum support wires. To increase the surface area and gain more emission current, spiral filaments were employed. Heating current was fed through copper wires, which were spot welded

Figure 3.4: Plasma control electrodes before the installation.

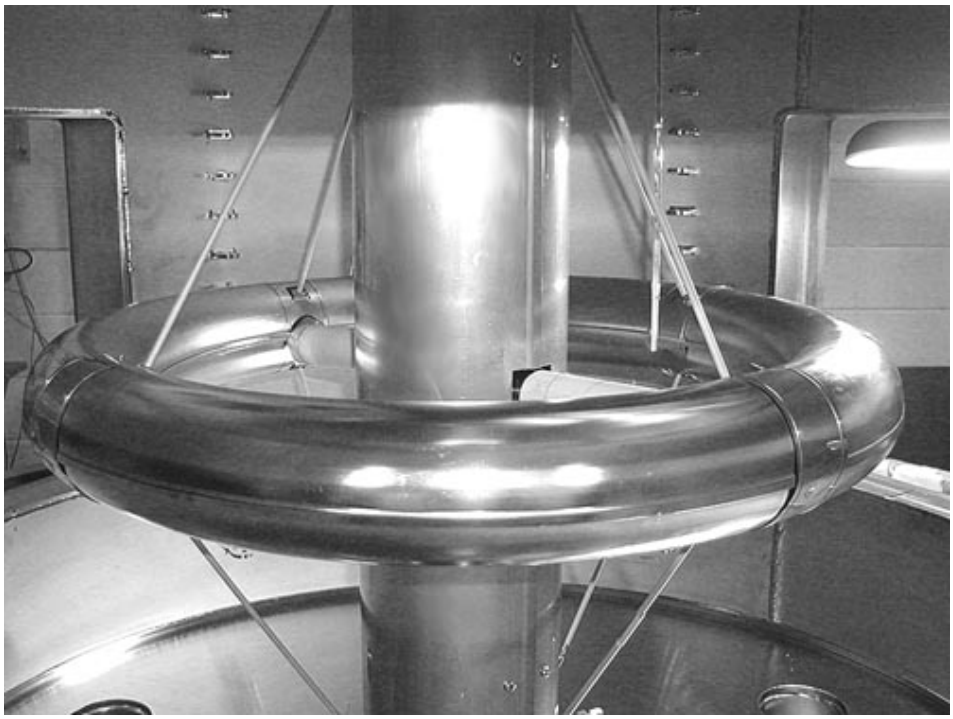

Figure 3.5: The setup of plasma control electrodes in Proto-RT. The IC (internal conductor) electrode are assembled from eight small parts, the CS (center stack) electrode from two larger parts in Fig. 3.4.

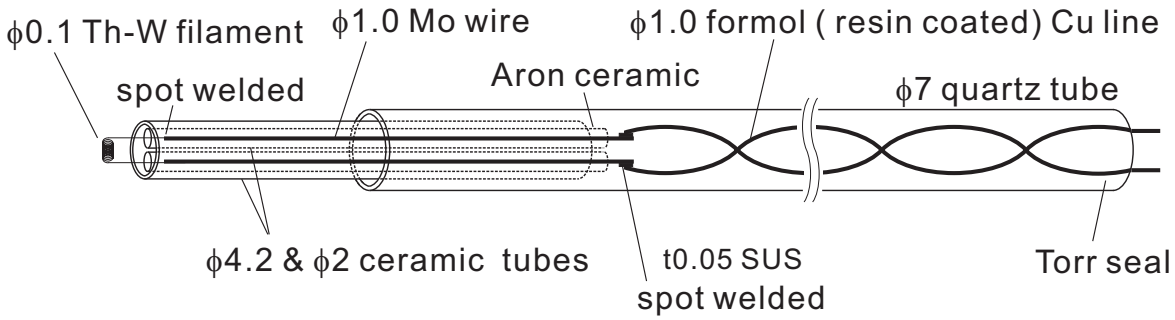

Figure 3.6: Construction of an emissive Langmuir probe. Thoria-tungsten filament was wound around ϕ 0.23 wire for 10 turns. To avoid the inflow of electron beam current along the insulator surface, molybdenum wire was covered with double ceramic (SSA-S) insulator tubes. The insulator was fastened to the quartz tube by a wedge of stainless steel foil.

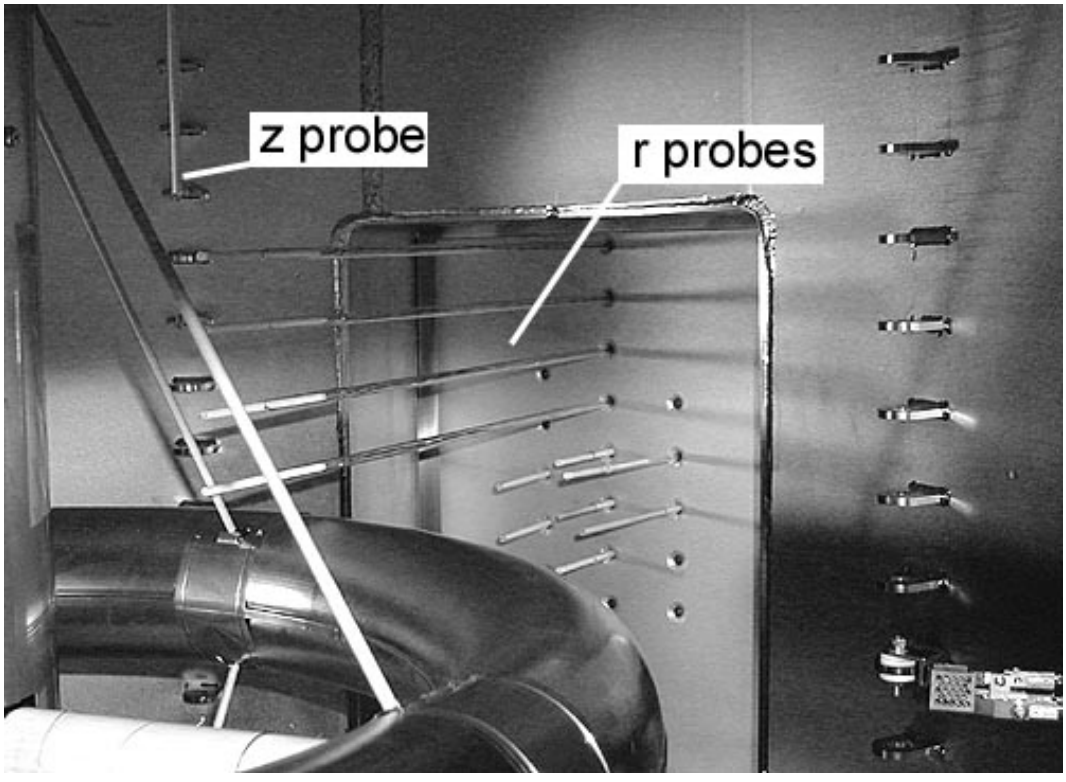

Figure 3.7: A picture of the emissive probe array configuration in Proto-RT. The electron gun is also seen on lower-right of the picture.

to molybdenum support wires. The support wires were covered with doubly ceramic tubes and loosely fitted in the inner tubes. This is for fear that if a conductive coating form on the surface of insulator, or high energy electron beam hit the insulator, the isolation might breakdown. Electrical shield of the probe was not necessary, because the high speed phenomena (e.g. plasma oscillations) are out of the scope of this thesis.

The density of the emission current J of heat electrons from materials are given by Richardson-Dushmann's equation;[19]

$$J = \eta A_R T^2 exp\left(-\frac{\phi_w}{k_B T}\right), \tag{3.1}$$

where k_B is Boltzmann's constant, $A_R \sim 120\ Acm^{-2}K^{-2}$ is Richardman's constant, T is temperature, ϕ_w is a work function of the material, and $\eta = 0 \sim 1$ is decided by the surface state of the material.

The required current for the heating of the filament was about 2 A. When this current is passed in an infinitely long Th-W filament, its temperature is $2800K$. The burn off temperature of a tungsten filament of $0.1\ mm$ diameter is about $3200K$, and enough emission current was obtained before this limit.

3.2 Emissive Langmuir Probe Diagnostics

Electrostatic, or Langmuir probes[20–22] are one of the fundamental and the first developed diagnostics of plasmas. Basically, the probe is a simple metallic tip, inserted into a plasma, and biased to some potential. Although probes might perturb the surrounding plasma, it can make local measurements of a particle energy distribution over a wide range of parameters.

In this study, emissive probes[21–23] were used for the measurements of plasma space potential V_S. As a tip of an emissive probe, a hot filament (heated by a passage of current) was employed instead of an usual cold metal piece. The principle of emissive probes is, that emitted electrons will escape from the probe only when the tip is more negative than V_S. The characteristics of emissive probes, its construction, and the usage for the measurements of potential structures are stated in this section.

3.2.1 Probe characteristics and interpretation

Cold probe characteristics

When a plasma has only single species of particles (electrons), the electron current density j into the probe is

$$j = e\int_{\infty}^{\infty} f(\mathbf{v})\mathbf{v}\cdot\mathbf{n}d^3v, \tag{3.2}$$

where $f(\mathbf{v})$ is electron distribution function, $\mathbf{n}$ is the normal to the probe surface. For simplicity, we assume planar probe surface in Cartesian coordinate,

$$j = e\int_{v_{min}}^{\infty} f(v_x, v_y, v_z) v_z dv_z. \tag{3.3}$$

Here $v_{min} \equiv [2e(V_s - V_b)/m_e]^{1/2}$, V_b is the probe bias voltage, V_s is the plasma space potential, and m_e is the electron mass. When the electron distribution is given by a drifting Maxwellian with temperature T_e and drift velocity v_d (in z direction, perpendicular to the probe surface):

$$f(\mathbf{r},\mathbf{v}) = n_e\left(\frac{m_e}{2\pi k_B T_e}\right)^{3/2} exp\left(-\frac{m_e(v_z - v_d)^2}{2k_B T_{\|}}\right) exp\left(-\frac{m_e({v_x}^2 + {v_y}^2)}{2k_B T_{\perp}}\right), \tag{3.4}$$

then the electron current collected by a planar probe is

$$I = eSn_e\left(\frac{k_B m_e}{2\pi T_{\|}}\right)^{1/2}\int_{v_{min}}^{\infty} exp\left(-\frac{m_e(v_z - v_d)^2}{2k_B T_{\|}}\right) v_z dv_z, \tag{3.5}$$

where S is the surface area of the probe. The current-voltage (I-V) curve given by (3.5) has a slope around $V = V_s - E_d/e$ ($E_d \equiv m_e {v_d}^2/2e$ is the energy of flow) with a temperature width of T_e, and takes constant values

$$I = \begin{cases} 0 & V \ll V_s - E_d/e \\ eSn_e\sqrt{k_B T/2\pi m_e} & V_s - E_d/e \ll V. \end{cases}$$

Here $I_s = eSn_e\sqrt{k_B T/2\pi m_e}$ is called the electron saturation current.

In the above simplified derivation, we used the assumption that the electron's motion is single dimensional, and all particles of higher velocity than v_{min} are certainly absorbed by the probe. In real plasmas, when the sheath is thick compared to the size of probes, the particle's orbital motion must be taken into the consideration. According to the orbital theory, derived by Langmuir and Mott-Smith,[20] the saturation current is an increasing function of V, in response to the probe shapes, and the I-V curve is an increasing function even when $V_s - E_d/e \ll V$. The typical characteristics of cold probe is shown in Fig. 3.8.

Emissive probes

When the probe tip is biased more negative than the local plasma space potential V_S, the emitted electrons can escape from the probe tip. In the probe characteristics, this electron flow contributes as an effective ion current. When the probe tip is biased positive with respect to V_S, however, the emitted electrons are repelled by the plasma and return to the probe. This behavior of electrons is not affected by the plasma flow (kinetic energy of particles), because it is decided by plasma potential. The typical characteristics of cold (non emissive) and hot (emissive) probes are shown in Fig. 3.8. The two characteristics separate from each other near the plasma potential V_s, and one can take it as an indication of the plasma potential. This is quite advantageous to the measurement

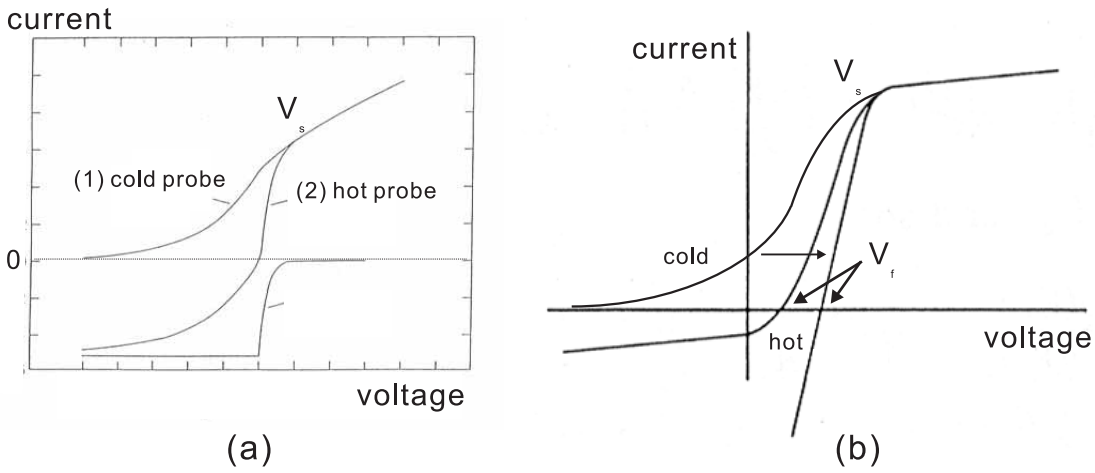

Figure 3.8: Schematic view of the characteristics of hot and cold probes. (a) The emission begins at the space potential of the plasma, but does not increase in an instant, because of the space charge limit. The horizontal part at $V < V_s$ is due to the limit of the filament current. (b) The relation between the space potential V_s and the floating potential V_f. As the emission current is increased, V_f approaches to V_s, but they do not agree due to the space charge limit.

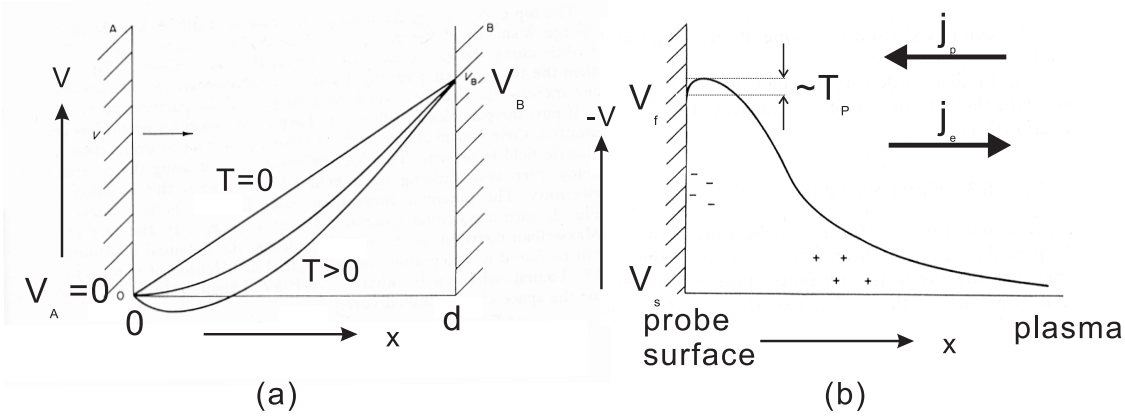

Figure 3.9: (a) Schematic graph of the Child-Langmuir's low. Electrons are emitted from the plane A (left) and escape to the plane B. Three curves are the potential profiles between two planes, according to the electron temperature T. (b) Double sheath formation between the emissive probe and the plasma. Because the emitted electron is space charge limited, there is a potential dip near the probe surface.

of space potential compared to the cases of cold probes, where the knee of I-V curve corresponds to the sum of the space potential and the flow energy.

When the probe filament is heated enough, the emission current is space charge limited, and its value is decided by the Child-Lngmuir low. In Fig. (3.9), we assume that electrons are emitted at plane A with an initial (at $x = 0$) velocity of zero toward the plane B: the particle velocity is $v(x) = \sqrt{2ev/m_e}$. Because the current density j is constant in this geometry, the number density $n(x)$ of electrons between two planes is

$$n(x) = -je^{-1}(2ev/m_e)^{-1/2}, \tag{3.6}$$

and Poisson's equation becomes

$$\frac{d^2V}{dx^2} = \frac{j(2eV/m_e)^{-1/2}}{\varepsilon_0} \tag{3.7}$$

Multiplying by dV/dx and integrating from $x = 0$, we have

$$\frac{1}{2}\frac{dV}{dx}^2 = \frac{j(2eV/m_e)^{-1/2}}{\varepsilon_0} + \frac{1}{2}\left(\frac{dV}{dx}\right)^2\Bigg|_{x=0} \tag{3.8}$$

Because the charged particles' flow is space charge limited at the filament, at $x = 0$, the gradient of the potential vanishes: $dV/dx|_{x=0} = 0$, and (3.8) becomes

$$V^{-1/4}dV = \left(\frac{2j}{\varepsilon_0}\right)^{1/2}\left(\frac{m_e}{2e}\right)^{1/4}dx \tag{3.9}$$

Integrating from $x = 0$ to d, the current density is given by

$$j = \left(\frac{2e}{m_e}\right)^{1/2}\frac{8}{9d^2}\varepsilon_0 {V_B}^{3/2}. \tag{3.10}$$

This is valid for the "cold" emitted particles (the $T = 0$ curve in Fig. 3.9 (a)). The derivation of more complicated cases, when the temperature T of the plate A is not negligible compared to the plasma, and the emitted particles have finite speeds at $x = 0$, was done by Langmuir:[20]

$$j = \left(\frac{2e}{m_e}\right)^{1/2}\frac{8}{9(d-x_m)^2}\varepsilon_0(V_B - V_m)^{3/2}(1+\alpha), \tag{3.11}$$

where x_m, V_m, and α are the correction terms.

The floating potential V_f of the emissive probe is decided by the balance between the collected current from plasma (j_p in Fig. 3.9 (b)) and emission current (j_e). Here j_p is decided by (3.5) and j_e by (3.11). From (3.11), the current emitted from the hot probe is

$$j = \left(\frac{2e}{m_e}\right)^{1/2}\frac{8}{9d^2}\varepsilon_0(V_f - V_s)^{3/2}, \tag{3.12}$$

and we see the current is not canceled when $V_f = V_s$. This fact must be taken attention when high impedance potential probes are used for the potential measurements: due to the space charge limit, the measured potentials do not agree with the space potential even when the probe filament is sufficiently heated. The validity of the measurements by high impedance potential probes was experimentally tested and will be discussed in subsection 4.1.

3.2.2 Electric circuit for large amplitude and fast sweep

Figure 3.10 is a basic circuit for Langmuir probe diagnostics. For the measurements of current-voltage (I-V) characteristics, current is given by a small resistor R_1 and voltage by R_3 (R_2 is a large resistor just for voltage dividing.). Two signals are observed by an oscilloscope, for example, through isolation amplifiers. If R_1 is small enough and line $I = -V/R_1$ is almost vertical, the voltage drop at R_1 is negligible.

When a DC voltage source is used, I-V characteristics must be obtained by a repeat of experiments by changing the voltage. To save this trouble, an AC power source is often used. In the experiments of a non-neutral plasma in Proto-RT, however, the simple circuit of Fig. 3.10 did not work. Because of the required large amplitude and fast sweeping, the effect of the stray capacitance between the probe and the chamber, C_1 in Fig. 3.10, is not negligible. In this case, there is no way to distinguish the current through plasma and current through C_1, by using of R_1 of the conventional circuit.

In proto-RT, the space potential of electron plasma is up to on the order of some *kilovolts* (and supposed to be less than an accelerating voltage of the electron gun: 2 *kV*), and accordingly, some *kilovolts* of sweeping is required. It is almost 100 times larger than the cases of many laboratory neutral plasmas, where the space potential is around several tens of volts. Another problem is due to the short duration ($\sim$ 10 *msec*) of the plasma. This time is decided by the heat capacity of the electron gun's anode, othewise the anode would melt. Consequently, the typical required amplitude and cycle of the sweeping is 1000 V and $f = 100$ Hz. The applied AC voltage V_C to a

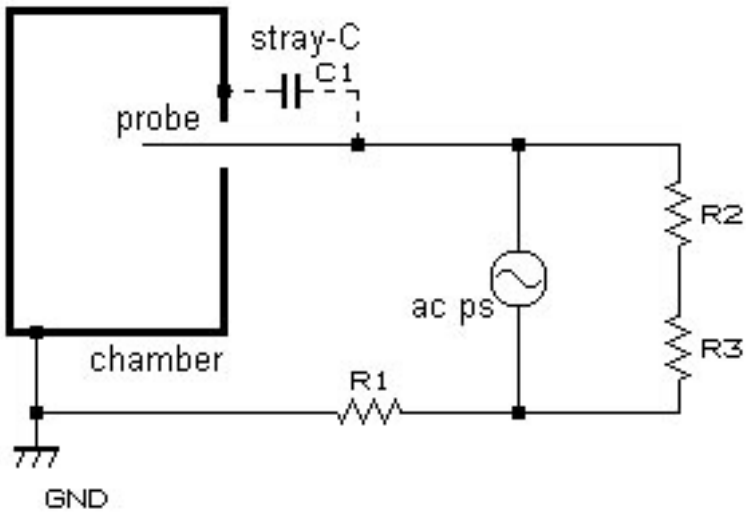

Figure 3.10: A simple probe circuit for the current-voltage measurement. The probe characteristic is obtained in one sweeping of the ac power source. The adverse effect of the stray capacitance C_1 is not negligible in high speed and large amplitude sweeping of the power source.

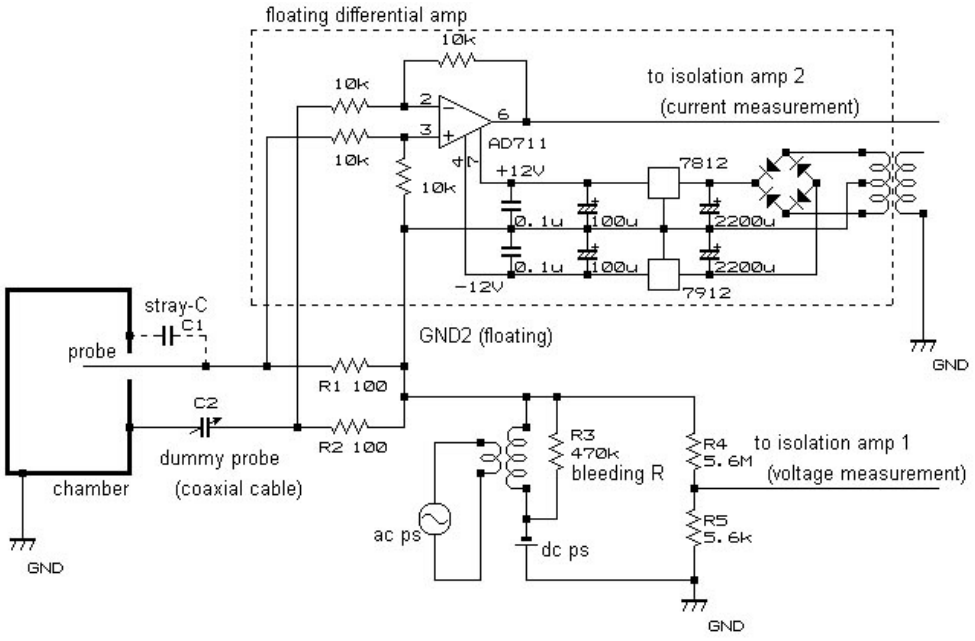

Figure 3.11: The improved probe circuit for high speed and large amplitude sweeping, used in the Proto-RT experiments. The variable capacitance C_2 (coaxial cables) is adjusted so as to cancel the current through C_1, the stray capacitance. The net current through the plasma is measured by a floating (i.e, the ground of the amplifier $GND2$ is floating with the plasma) differential amplifier.

capacitance of C is

$$V_C = \frac{1}{i\omega C} I_C, \tag{3.13}$$

where I_C is current, ω is angular frequency, and i is imaginary number. When $V_C \sim 1000\ V$, $f = \omega/2\pi \sim 100\ Hz$, and assuming $C \sim 100\ pF$ (approximately equivalent to the capacitance of coaxial cable of 1 m long), then the noise current through the stray capacitance C_1 is $I_C \sim 10^{-4}\ A = 0.1\ mA$. Compared with the typical current from a plasma: $\sim 1\ mA$, the adverse effects of the stray capacitance is quite large.

Figure 3.11 is the improved circuit for large amplitude and fast I-V characteristics measurements. The idea of this circuit was originally given by Chen.[21] In this circuit, a dummy probe (some kind of high voltage-proof capacitance, e.g, coaxial cable) C_2 and floating differential amplifier was used. By choosing a proper capacitance C_2, the current through C_1 is canceled by the same amount of current through C_2, then the measurements of the current only from plasmas is possible. The effect of the noise reduction by this circuit is given in Fig. 3.12; (a) is a *net* noise current signal by the simple circuit. The observed noise current of $V_{p-p} \simeq 0.92\ mA$ is close to the calculation done by the above assumption of $C \sim 100\ pF$. In (d), the noise current was decreased to 10 times smaller than (a). The I-V characteristics obtainded by using of this circuit will be shown in subsection 4.1.

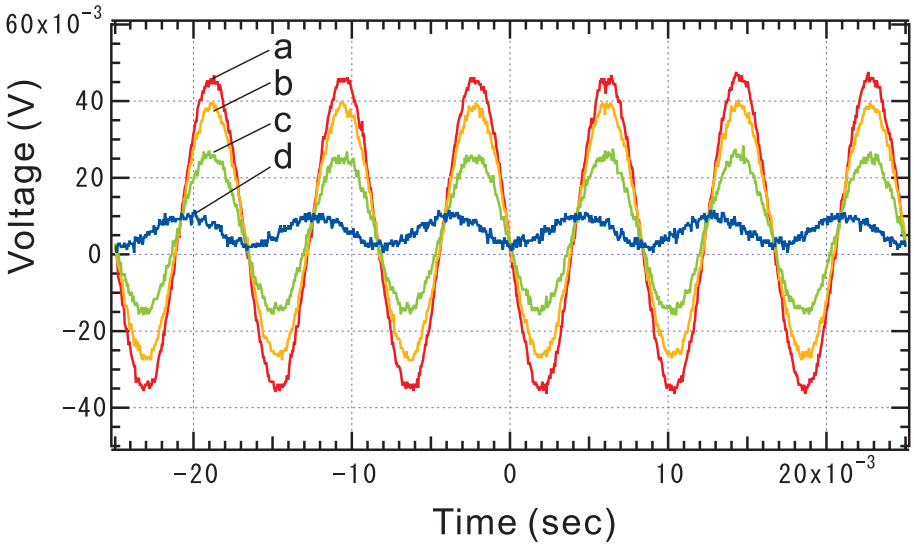

Figure 3.12: The effect of noise reduction by the improved probe circuit. The output curves of the isolation amplifier 2 in Fig. 3.11 (the current measurement) are given. The ac power source of $V_{p-p} = 1200\ V$, $f = 120\ Hz$ is applied, without plasma, then the noise current through the stray C is appeared. As a canceling capacitance C_2, *b*: 0.2 *m*, *c*: 0.5 *m*, *d*: 1.0 *m* length of coaxial cable is used, and *a*: without the noise reduction. Current measurements was done by $R_1 = 100\Omega$

3.2.3 Electric circuit for high impedance potential probe

As implied in the previous subsection, when the large enough resistance is used, the potential Φ_H measured by high impedance probes almost agree with the floating potential V_f. Then when the probe filament is heated enough and V_f approaches to the space potential V_s, we might be able to use the value of V_f as an approximate value of V_s. The potential decision by high impedance probes is very attractive, because it is much simpler and easier than the measurements of I-V characteristics. The circuit used in this study is shown in Fig. 3.13. We employed high voltage probes of 100 $M\Omega$. The comparison of V_s and V_f and the validity of high impedance potential probe will be discussed in subsection 4.1.

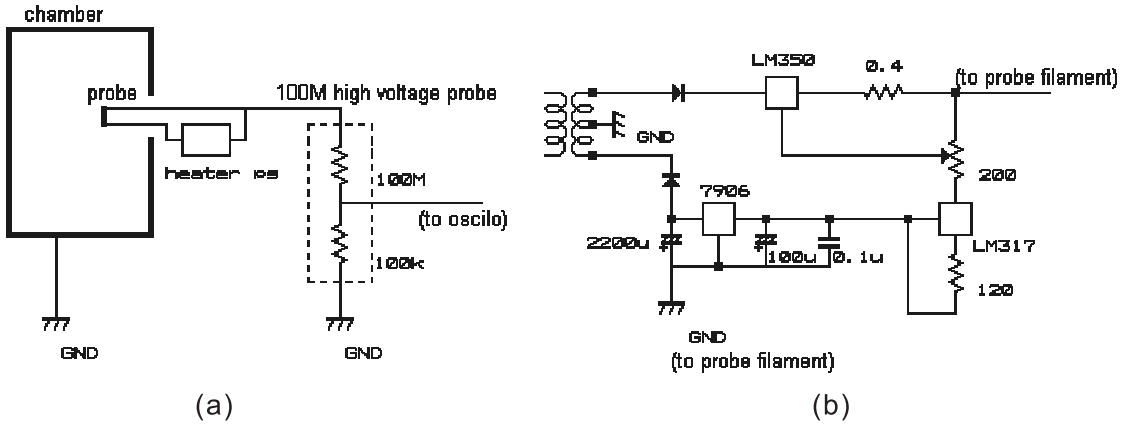

Figure 3.13: High impedance potential probe circuit

Chapter 4

Experimental results and discussions

Potential structures of a toroidal non-neutral plasma were measured in Proto-RT. The obtained potential profiles show a tendency of diffusion from the beam orbit toward the confinement region of the torus. Although the shift toward the strong magnetic field region (”paramagnetism”) and toward the major axis of the torus, of the electron cloud was observed, but the shape of potential profiles does not agree with the numerical calculations from equilibrium model. It is supposed to be due to the perturbation by support rods, beam component of the plasma, and the localized position of the particle source.

The effects of external electric fields generated by plasma control electrodes were examined. The results showed that the potential structures of the toroidal electron plasma were controlled according to the applied external potential.

Prior to the measurements of plasma structures and its control described above, the validity of measuring method in this study will be discussed. It was shown that the potential measured by the high impedance-emissive probe can be regarded as an approximate value of the space potential.

4.1 Measurement of space potential

When the probe tip emits enough electrons, the floating potential V_f of an emissive probe will approach to the space potential V_s of the plasma. By choosing a proper high impedance probe, it was shown that the measured potential Φ_H can be approximately regarded as V_f. When the high impedance potential probes are used, the experimental procedure is simpler and easier than the measurements of the I-V characteristics. The validity of this method was examined in a non-neutral plasma.

4.1.1 Floating potential of high impedance probes

Typical measured probe characteristics of cold and hot probes are given in Fig. 4.1. The two characteristics began to separated at a certain biased voltage V_b to the probe, which is supposed to be a space potential V_s, as discussed in Section 3.2. Even when V_b is negative with respect to V_s,

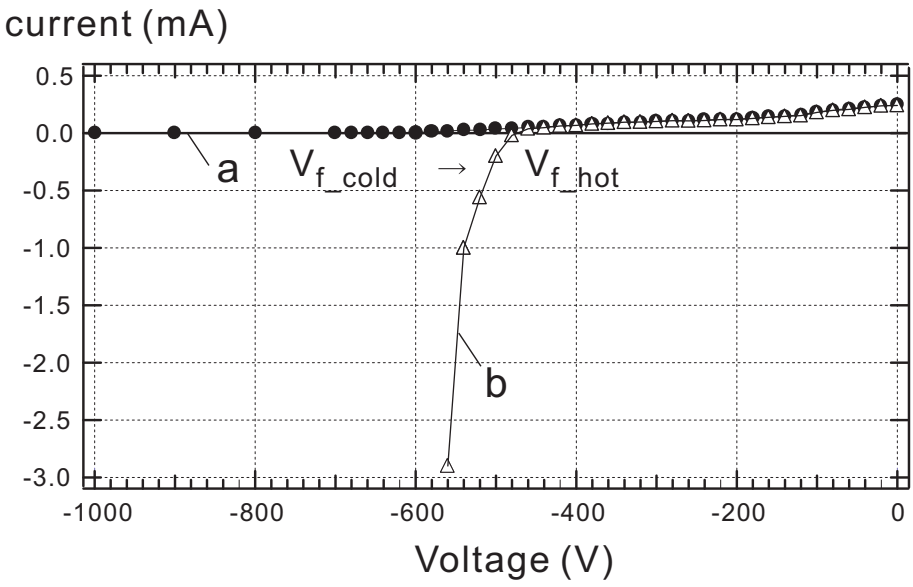

Figure 4.1: Typical characteristics of a: cold (non emissive) and b: hot (emissive) probes. When the probe is heated, the floating potential V_f increased, as described in the graph.

the emission current did not take a constant value immediately, because of the space charge limit (Child Lnagmuir's low).

The value of an high impedance (R) potential probe Φ_H is given by the intersection of the probe characteristics and the work curve $V = -RI$. For $R = 100\ M\Omega$, used in this study, the work curve is almost horizontal in the voltage-current graph ($I = 0.01\ mA$ at $V = 1000\ V$, see Fig. 4.1), and Φ_H were supposed to approach very close to the floating potential V_f.

4.1.2 The comparison of Φ_S and Φ_H

In order to see the required heating of the probe filament for the emission current, the relation between the heating current I_h and the measured Φ_H was tested (Fig. 4.2). The potential measured by the high impedance probe with no emission was $\Phi_H = -1240\ V$ in this experiment. The effect of emission began at around $I_h = 1.0\ A$ and the potential rapidly dropped. When the probe is heated enough (approximately more than $I_h = 1.9\ A$), the measured potential approached to the constant value of $\Phi_H \simeq -750\ V$. Here the emission current was space charge limited.

The required filament heating current was tested for all the emissive probes used in the experiments. Although the required current of each probe was not equal, maybe due to the small differences in their construction, but all the I_h-ϕ_H curves saturated at a certain values I_{h-sat} of each probe. In the following experiments, these I_{h-sat}s were used for the heating of the probe filament.

The comparison of the I-V characteristics and the potentials measured by the high impedance probe is shown in Figs. 4.3 and 4.4. The high impedance-measured potential Φ_{H1} of emissive probe does not agree with the space potential Φ_s due to the space charge limit, as predicted before,

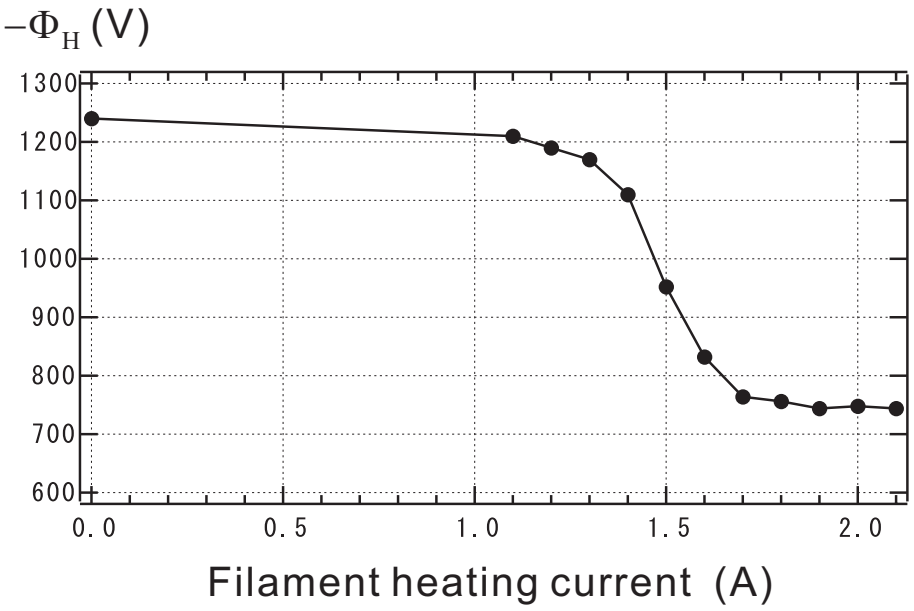

Figure 4.2: Φ_H, the potentials measured by the high impedance probe, and the heating current in a probe filament. When the filament was heated enough, $|\Phi_H|$ does not decrease anymore, due to the space charge limit of the emission current.

but the Φ_{Hhot} comes quite close to Φ_s, and we can see that it is possible to find the approximate value of the space potential by the high impedance potential emissive probe.

The question in these figures is that, although Φ_H of the cold probe agreed with the floating potential, $|\phi_H|$ of the emissive probe was larger than the floating potential. It is possibly caused by the difference of the emission current according to the circuit configuration.

The potential drop by the emission (Φ_{Hcold} to Φ_{Hhot}) was especially large when the probe is hit by the electron beam (Figs. 4.3 and 4.4). Because the I-V characteristics curve of the cold probe is affected by both the space and kinetic energy[24] (See subsection 3.2), the I-V curve does not approach to the horizontal axis, until the probe is biased to the potential corresponding to the sum of the space potential and the flow energy. To summarize, the potential measured by an high impedance probe by using an emissive probe Φ_{Hhot}, is fairly close to the space potential of the plasma, and we can regard Φ_{Hhot} as approximate values of space potential. Especially when the shapes of the plasma, rather than the values of potential, are subjects of concern, this method is valid and, the measurements can be done much more quickly than the characteristics measurements. In the following subsection, the potential profiles were mainly taken by the high impedance emissive probes. The example of potential profiles taken by cold and hot probes are shown in Fig. 4.5.

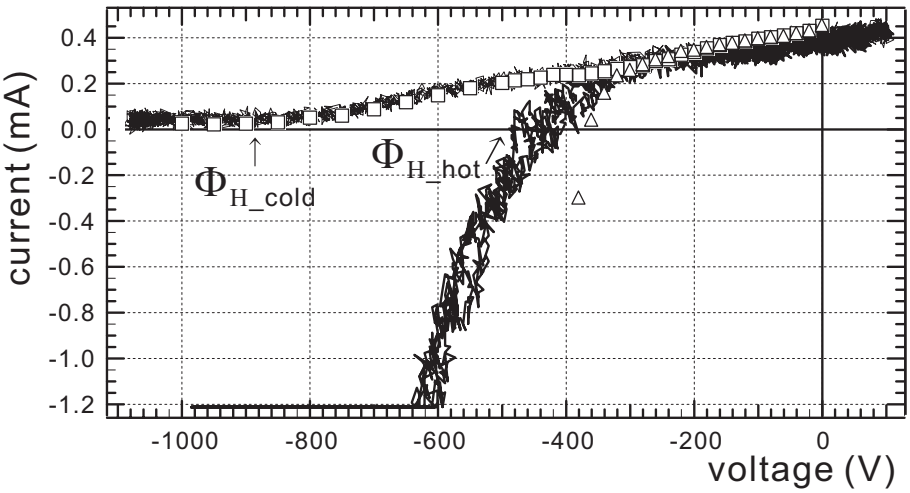

Figure 4.3: Typical probe characteristics of cold and hot Langmuir probes 1: in the dipole magnetic field configuration (the ratio of I_{IC} (Internal conductor coil current) and I_{TF} (Toroidal field coil current) was 1 : 0). In this case, the emissive probe was located in the orbit of electron beam. The space potential is read $V_s = -460\,V$, from the intersection point of two curves. Potentials measured by high impedance probes are also given in the figure; $\Phi_{Hcold} = -610\,V$: by the cold probe, and $\Phi_{Hhot} = -554\,V$: by the emissive Langmuir probe. Due to the beam component of the plasma, the characteristics has a long tail, and consequently, $|\Phi_{Hcold}|$ is much larger than $|\Phi_{Hhot}|$.
The continuous characteristics of Figs. 4.3 and 4.4 were taken by the probe circuit for large amplitude and fast voltage sweep, discussed in subsection 3.2.2 (Fig. 3.11). The AC characteristics almost agreed with the conventional DC characteristics (ploted).

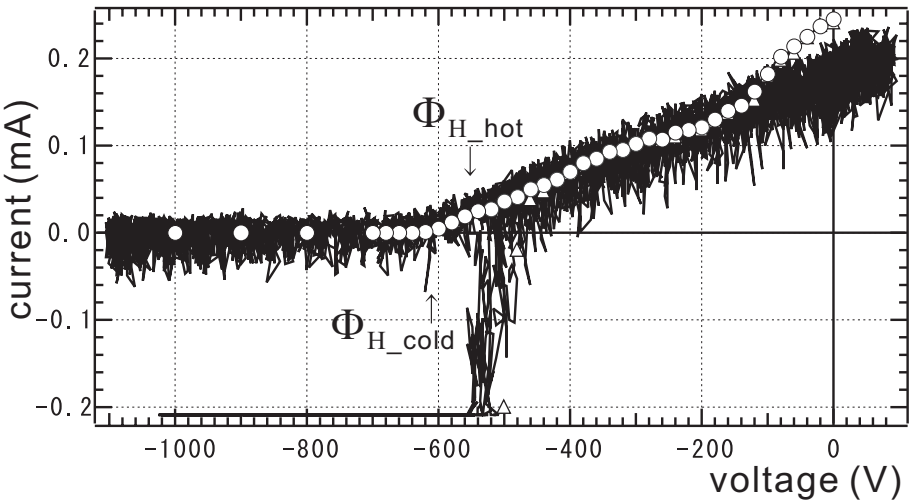

Figure 4.4: Typical probe characteristics of cold and hot Langmuir probes 2: in the dipole plus toroidal magnetic field configuration. ($I_{IC} : I_{TF} = 1 : 4$). The beam orbit did not hit the probe in this case. $V_s = -310\,V$, $\Phi_{Hcold} = -884\,V$, and $\Phi_{Hhot} = -488\,V$. Because there is no beam component of the plasma, the difference between Φ_{Hcold} and Φ_{Hhot} is relatively small.

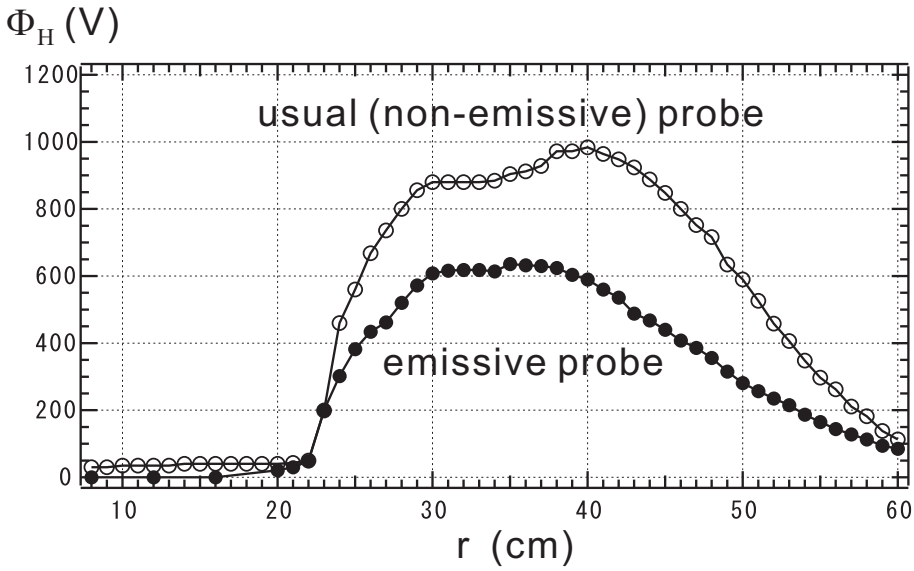

Figure 4.5: Typical potential profiles measured by emissive and non-emissive probes

4.2 Potential Structure in Proto-RT

In Proto-RT, the injected electrons gradually diffuse from the beam orbit, and supposed to form a magnetized bulk component of the plasma, taking a collective behavior. To confirm the bulk component of the plasma and to grasp its structure, the potential profiles were measured by the emissive probes.

The measurements showed that the electrons spread to the confinement region, apart from the original beam orbit. However, the obtained potential structures still depended on the trajectory of the beam electrons. This tendency became clearer, when the profile was compared to the equilibrium calculation by the drift model. The plasma was concluded to be composed of both beam and bulk electrons.

4.2.1 Basic properties of the potential structure

The measuring points and the typical potential profile in Proto-RT is shown in Fig. 4.6. (More detailed experimental configuration was shown in Fig. 3.2.) Due to the configuration of the gauge ports for probe insertion in Proto-RT, the measurement area was verticality limited to $z = -20 \sim +20$ *cm*. However, this is not a serious problem, because the measuring points at $z = 20$ *cm* are almost outside of the closed magnetic surface of the dipole magnetic field configuration, mainly used in this study. (It will be discussed later in this subsection.) As shown in the figure, the obtained values of potential was quite close to 0 at $z = 20$ *cm*. For the simplification of the experiments, only the top half of the region ($z = 0 \sim +20$ *cm*) was choose for the measuring object, assuming the symmetric property of the plasma.

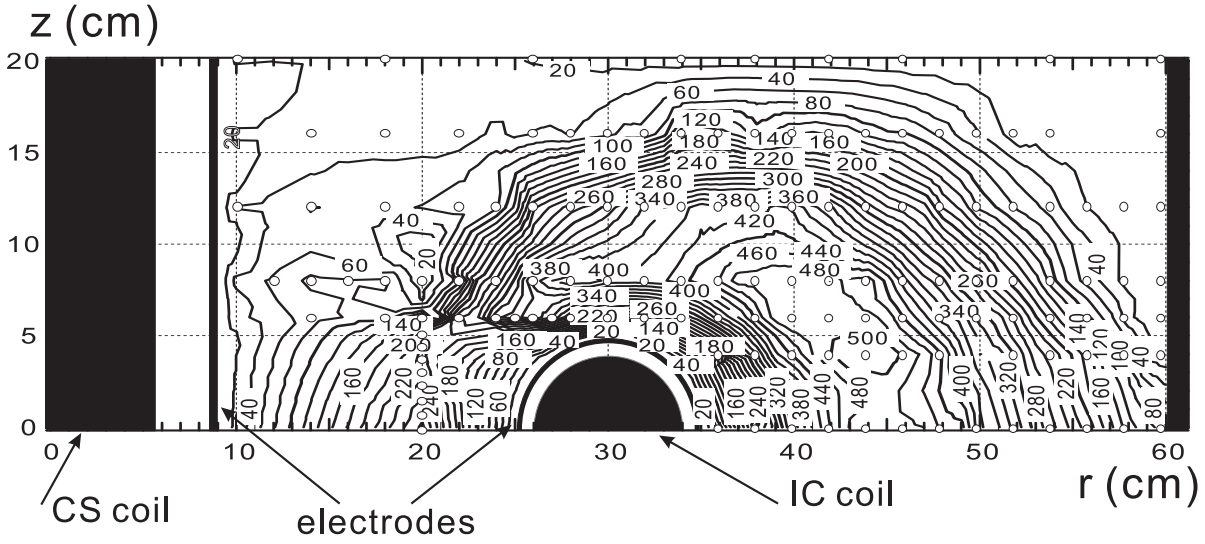

Figure 4.6: A typical potential profile and the measuring points (○) on the poloidal cross section of Proto-RT. The electron gun is located at $r = 46.5\ cm$, $z = 0\ cm$. Both electrodes were grounded to the chamber. The corresponding number density of the plasma was around $10^{13}\ m^{-3}$. Due to the drift motion and the beam orbit, the potential structure of the electron is surrounding the IC (internal conductor) coil. As compared with the injection point of electrons, the plasma was shifted toward the major axis of the torus (see section 2.2).

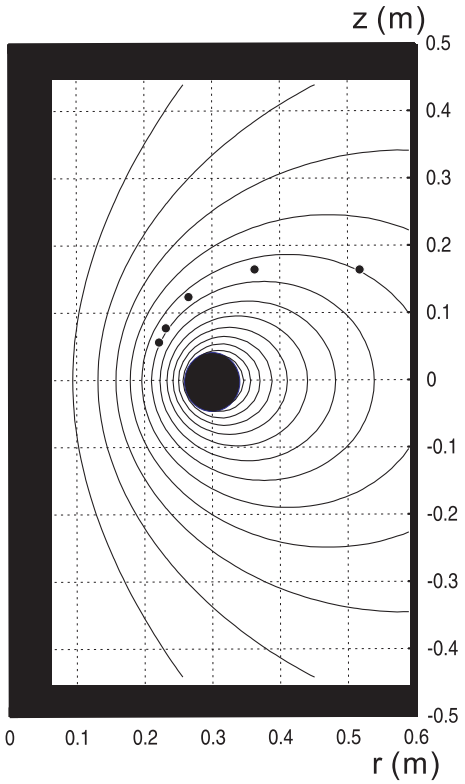

Figure 4.7: Magnetic surface of the dipole magnetic field configuration. The dots are located at $(r\ (cm), z\ (cm)) = (22,6),(23,8),(26,12),(32,16),(52,16)$, where the potential drop was observed. The plasma is confined in the closed magnetic surface.

Because the inside surface of the diagnostic flange is located at $r = 65$ *cm*, the potential is not necessarily equal to 0 at $r = 59$ *cm*: the inside diameter of the chamber. Potential contours were composed from the grid data by the triangle conjecture method of a data analysis software IGOR Pro (WaveMetrics Inc.). The grid data were measured by the high impedance emissive probes, in the manner described in the previous subsection. The intervals of the grid was 1 or 2 *cm* in the radial (*r-probes*) and the vertical (*z-probe*) direction. As the both electrodes are shorted to the ground (chamber), the potential structure of surrounding the IC electrode was formed in this case. The profile has a steep gradient near the IC electrode, where $V = 0$.

Inside of the IC conductor, a steep drop of the potential was observed at $r = 22$ *cm* ($z = 6$ *cm*), $r = 23$ *cm* ($z = 8$ *cm*), $r = 26$ *cm* ($z = 12$ *cm*), and $r = 32$ *and* 52 *cm* ($z = 16$ *cm*). (The potential profile of each probe will be shown in Figs. 4.10 and 4.11.) As compared with the magnetic surfaces of the dipole magnetic field (plus toroidal field) configuration, shown in Fig. 4.7, these positions agree with the outer shell of the closed magnetic surface. It shows that the plasma was confined in the closed surfaces of the magnetic fields. When the experimental results are compared with the numerical calculations, the effects of the particle loss toward the vessel wall, which is not included in the calculation, must be taken into the consideration.

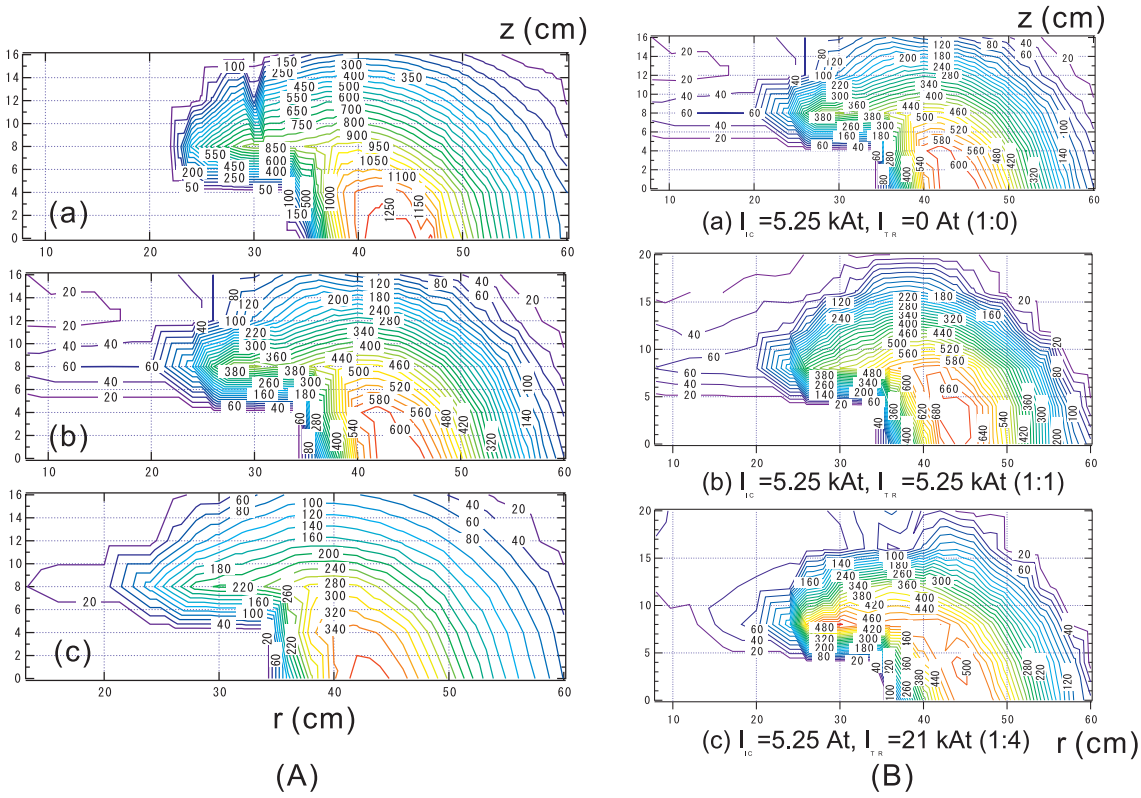

Figure 4.8: (A) Potential profiles Φ_{Hcold} in the variations of acceleration voltages $V_{acc}$of the electron gun. V_{acc} is equal to (a) 2000 V, (b) 1000 V, and (c) 500 V. (B) Potential profiles in the different strength of the toroidal magnetic field.

Figure 4.8 is the potential profiles in the variation of (A) the electron gun's acceleration voltage and (B) the magnetic field configuration. When the electrons were injected by lower acceleration voltages, the observed potential had a spread profiles toward the major axis of the torus. We can see that, when the beam's contribution to the potential profile is small, the inward shift of the plasma remarkably appeared. It implies that the electron cloud is the mixture of the beam component and the bulk component plasma, generated by the diffusion from the beam orbit. The plasma also shifted toward the strong magnetic field region, as discussed in subsection 2.2. When the toroidal field of $1/r$ profile was added to the dipole field configuration, the plasma shifted toward the major axis, where the toroidal field was stronger. This effect of "paramagnetism" will be discussed in the following subsection.

4.2.2 The effect of magnetic fields on the profile

The potential profiles taken by the each emissive probe of the array are shown in Figs 4.10 and 4.11. Two kinds of magnetic field configurations were applied, dipole field (the coil current I_C was 5.25 kA), and (b) dipole field ($I_C = 5.25$ kA) plus toroidal field ($I_C = 21$ kA) configuration.

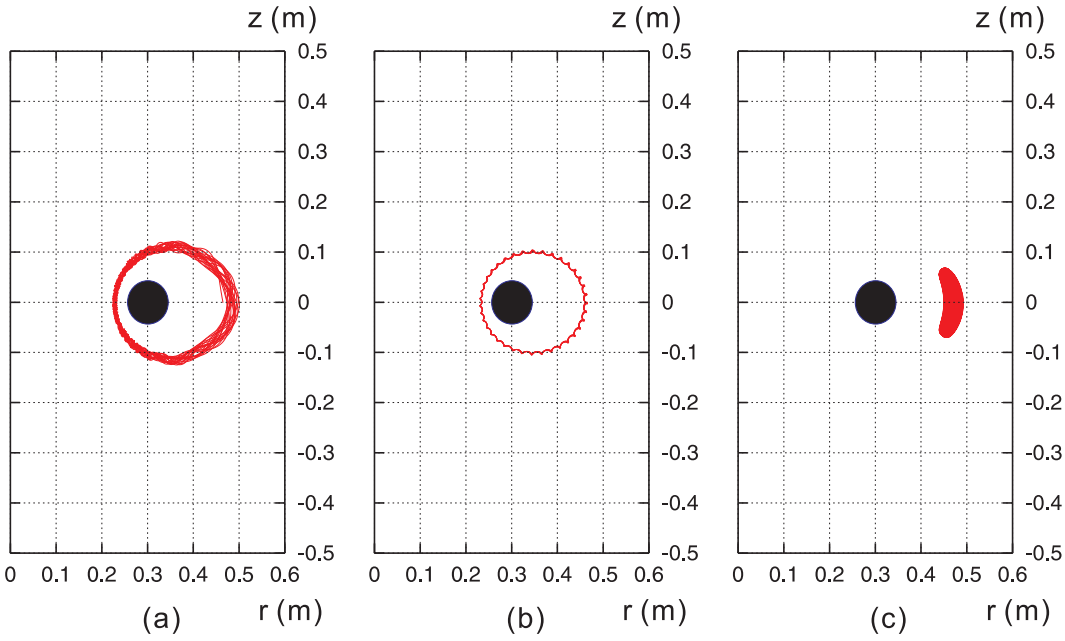

Figure 4.9: The electron's orbit in Proto-RT when the electron gun is located at $r = 46.5cm$. The magnetic field configuration and the direction of the injection were, (a) dipole configuration, 90°, (b) dipole + toroidal (the current ratio was 1:4) configuration, 180°, and (c) dipole + toroidal (1:4) configuration, 90°, respectively.

In order to equalize the effects of the beam component and clarify the profiles of the bulk component plasma, the profiles were measured in the conditions of different injection directions. The trajectory of the electron, in each magnetic field configuration and the direction of the injection, is given in Fig. 4.9. We see that the trajectories of (a) and (b) are quite similar, although the magnetic field configurations are different. These orbits correspond to the profiles of 4.10 (1) and 4.11 (2), respectively. The two dimensional profiles are also shown in Fig. 4.12.

Because the electron cloud was surrounding around the IC electrode, two kinds of peak were seen on the profiles at $z = 6$ *cm* and 8 *cm*. The inside peak ($r \simeq 26$ *cm*) is smaller than the outside one ($r \simeq 45$ *cm*) in 4.10 (1). However, when the strong toroidal magnetic field was added to the dipole field, the potential profile shifted inward, and the inside peak became as large as the outside one. As the orbits of electrons were approximately same for both cases, the observed inward shift of the potential profile, toward the strong magnetic field region, was supposed to be reflecting the structure of the bulk plasma. It shows that the electrons diffused from the original orbit of the injection.

The potential profile when the electron's orbit is given in Fig. 4.9 (c) is described in Fig. 4.10 (2) and in Fig. 4.13. In this case, the strong toroidal magnetic field was applied, and the orbit of the electrons was not transit: the trajectory of the beam is confined outside of the IC electrode near the electron gun as shown in the graph of the orbit. The potential profile of typical beam distribution, when the electron does not take a transit orbit, is shown in Fig. 4.14; when the particles are located

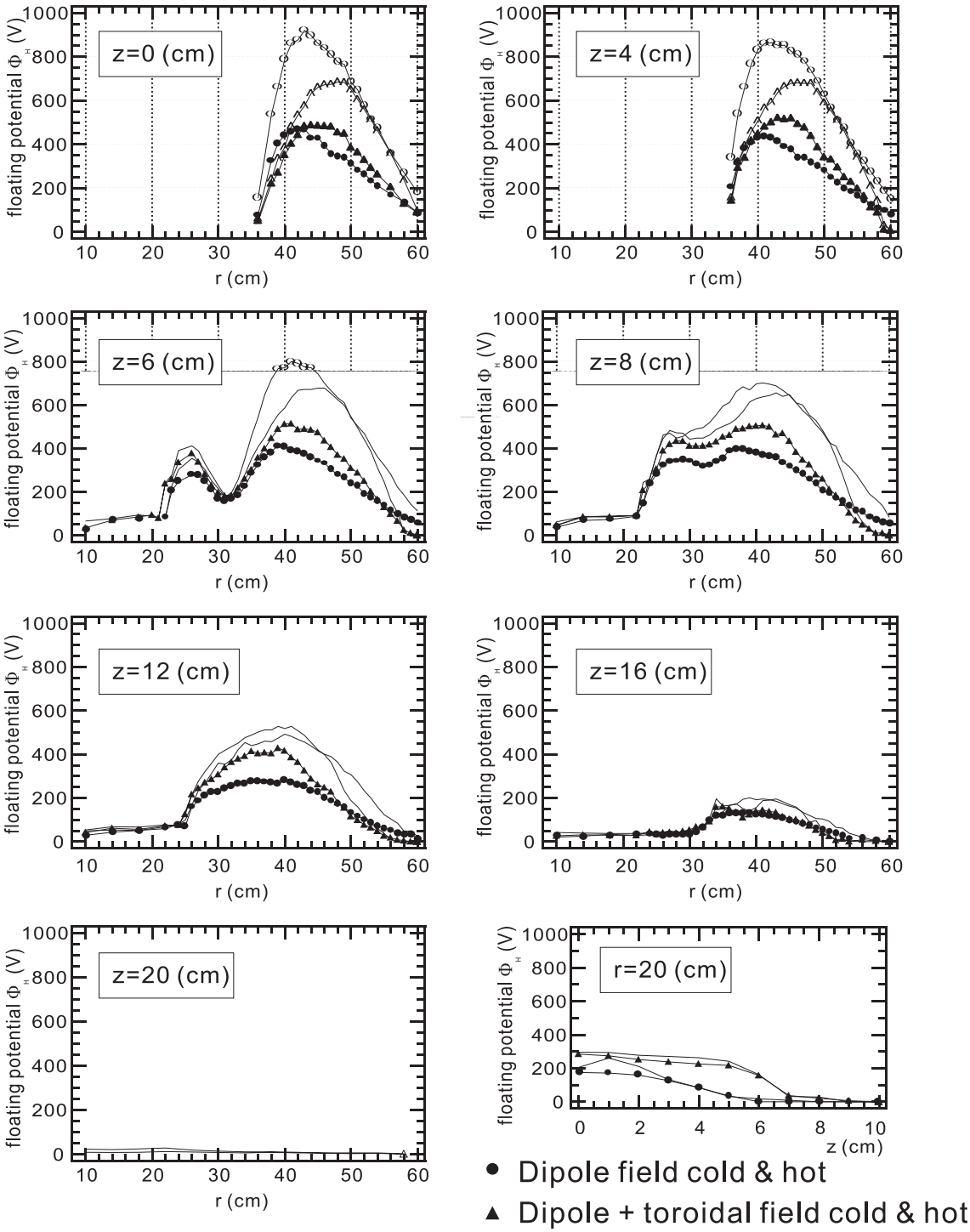

Figure 4.10: 90° injection. Potential profiles of all probes when the electrons were perpendicularly (in the direction of $\hat{z}$) injected. The magnetic field of (a) dipole (5.25 *kA*), and (b) dipole (5.25 *kA*) plus toroidal (21 *kA*) were applied. The potential profiles Φ_H measured by cold and hot (emissive) probes are shown.

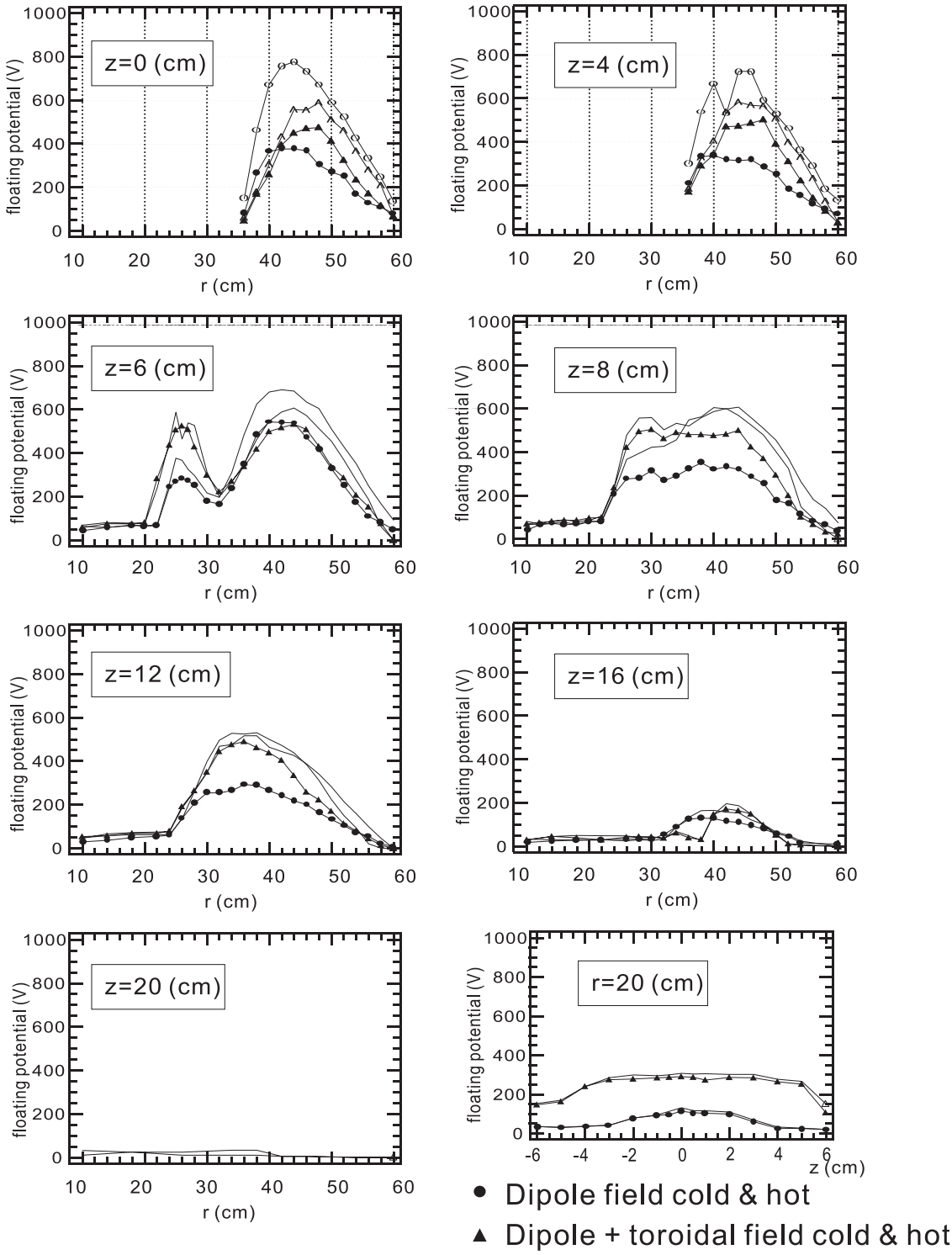

Figure 4.11: 180°. Potential profiles when the electrons were horizontality (in the direction of $\hat{\theta}$) injected vertically. The other conditions are same as those in Fig. 4.10. The magnetic field of (a) dipole (5.25 *kA*), and (b) dipole (5.25 *kA*) plus toroidal (21 *kA*) were applied.

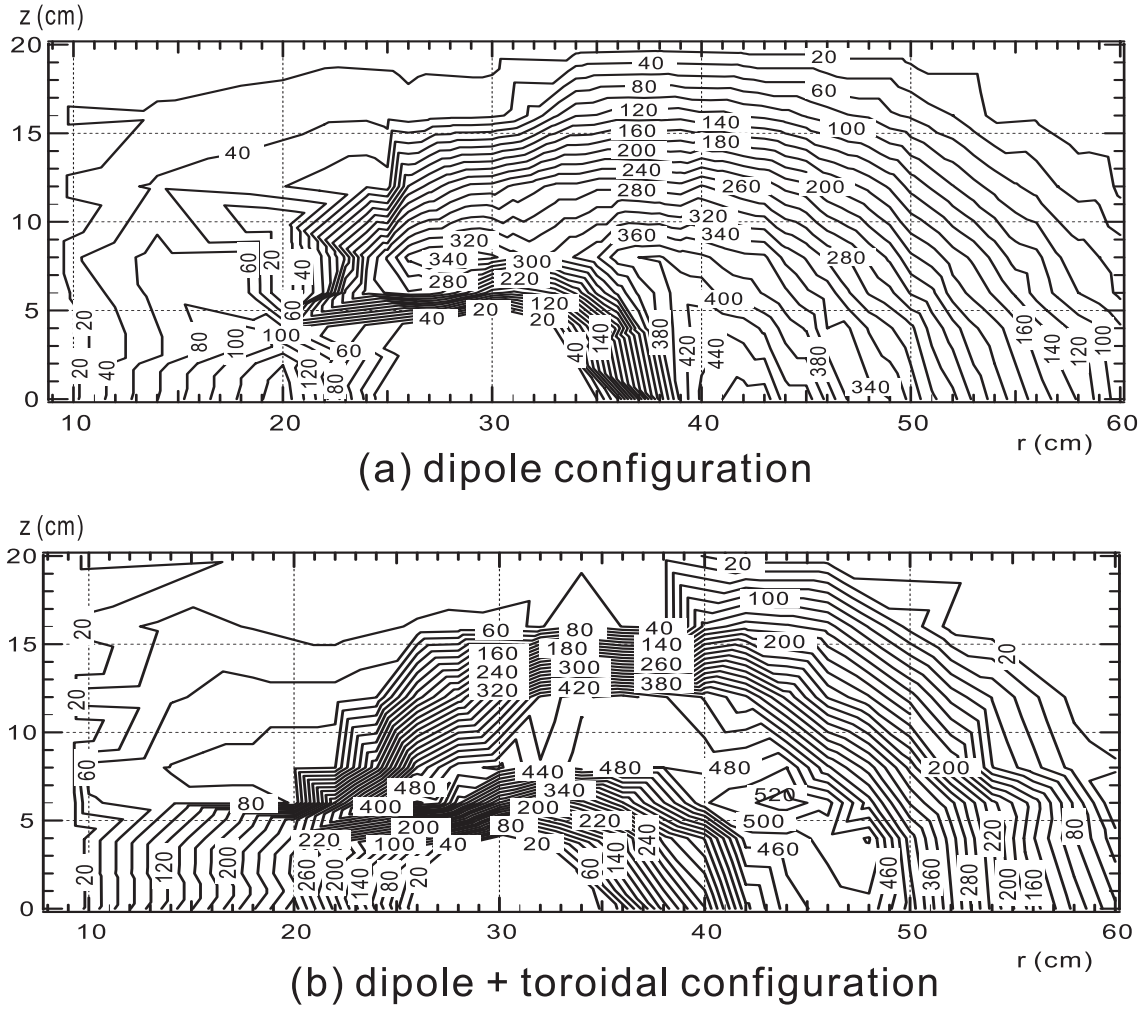

Figure 4.12: The plasma shift toward the strong magnetic field region. The potential profiles in (a) the dipole (5.25 *kA*), and (b) the dipole (5.25 *kA*) plus toroidal (21 *kA*) magnetic field configuration. They were composed from Figs. 4.10 (1) and 4.11 (2). Although the beam orbits take similar transit trajectories around the IC electrode, the plasma shifted toward the strong magnetic field region. The orbit is shown in Fig. 4.9 (a) and (b).

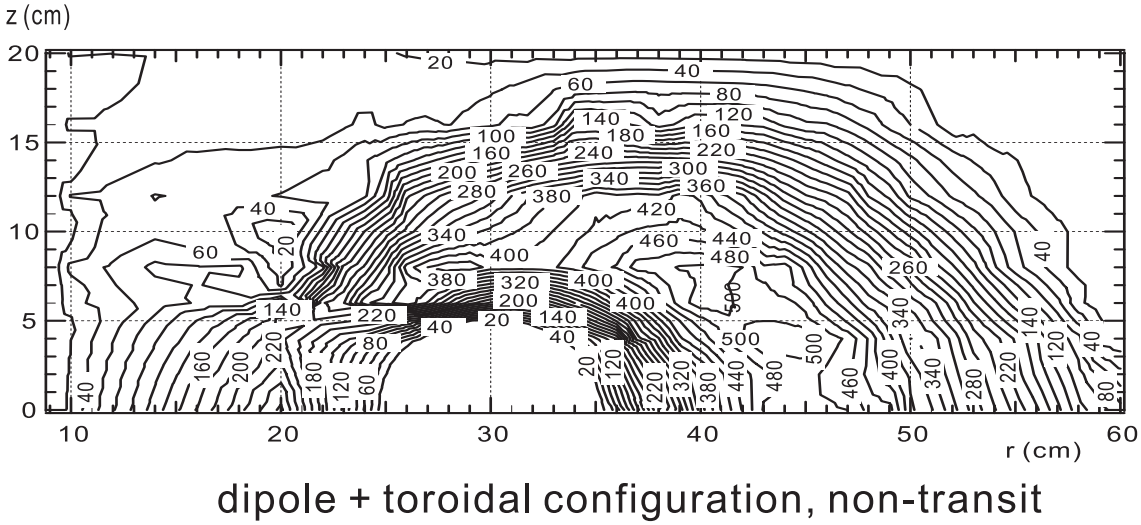

Figure 4.13: The potential profile when the beam orbit is not transit. The configuration of dipole (5.25 *kA*) plus toroidal (21 *kA*) magnetic field was applied. The injection direction was 90°. It corresponds to the beam orbit of Fig. 4.9 (c), and Fig. 4.10 (2). The potential does not agree with 4.14 (c), showing the existence of the bulk plasma.

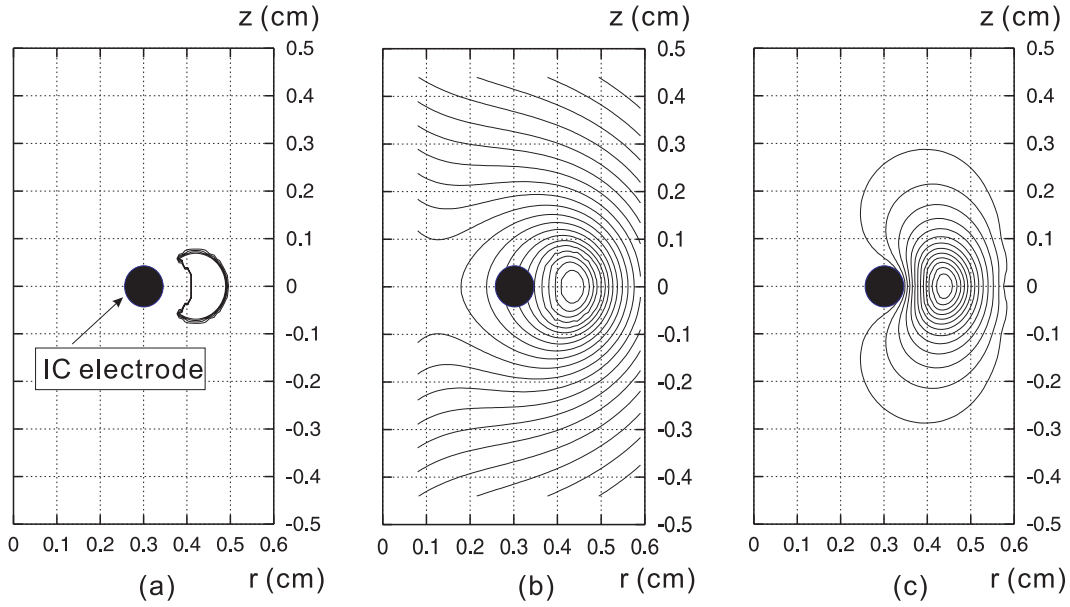

Figure 4.14: The potential profile calculated from the distribution of beam electron. (a) The typical electron distribution of the beam orbit, when the trajectory is not transit around the IC electrode. (b) Corresponding space potential and (c) the total potential, the sum of the space and image charges in Proto-RT. When the particles are located outside of the IC electrode, the potential does not take a surrounding structure around the IC electrode.

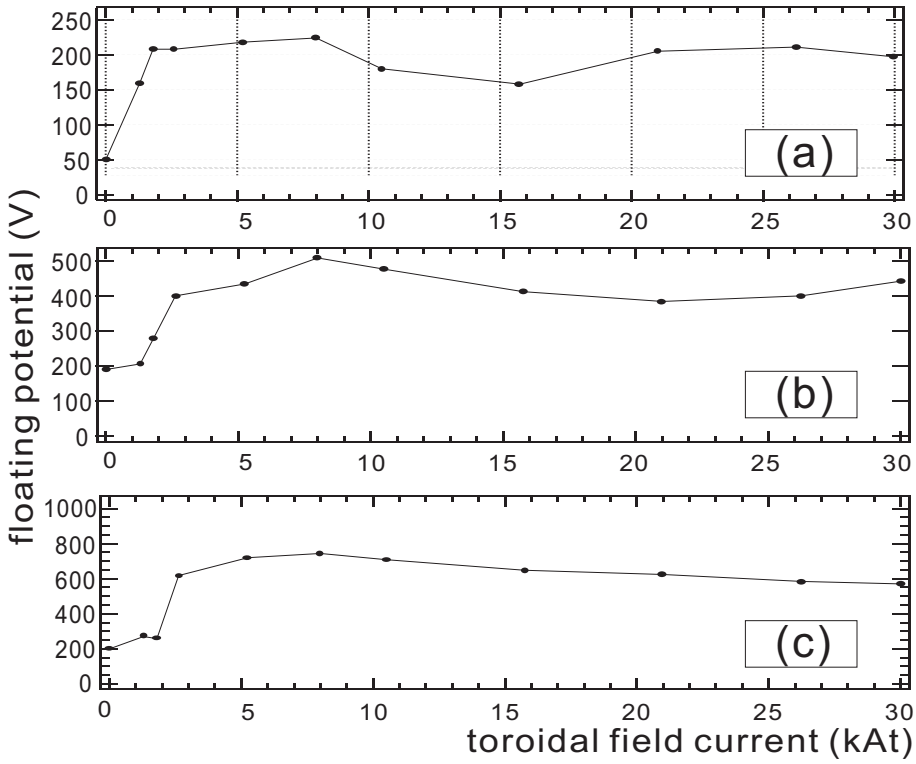

Figure 4.15: The potential inside the IC coil, at $r = 20\ cm$ and $z = 0\ cm$. The magnetic configuration was dipole field (coil current $I_C = 5.2\ kA$, a constant value) plus toroidal field, in a variation of the coil current. The acceleration voltage of the electron gun is (a) 500 V, (b) 1000 V, and (c) 2000 V. In this configuration, the beam orbit is not transit when the applied toroidal magnetic field is weak (the toroidal field current $\sim\leq 10\ kAt$). However, the potential signal (supposed to be a bulk component of the plasma) always reached to the inside of the IC electrode.

outside the IC electrode and does not take the transit orbit, its potential profile is also limited outside the IC electrode. In the measured potential profile in Fig. 4.13, however, the potential structure was surrounding around the IC electrode due to the contribution of the bulk component of the plasma. The same tendency was also seen in Fig. 4.15.

4.2.3 Potential control by the electrodes

The effects of the external electric fields on the potential structure were tested. Figure 4.17 (a) $\sim$ (c) is the potential profiles at $z = 0\ cm$, when positive and negative potentials were externally applied to the internal conductor (IC) electrode (The experimental set up was described in Fig. 3.2, in section 3). The external fields penetrated into the electron plasma and the each profile shifted according to the given potential. When the applied potential was $V_{ele} = -350\ V$, the peak value of the potential V_{peak} was smaller than the acceleration voltage. ($|V_{acc}| < |V_{peak}|$)

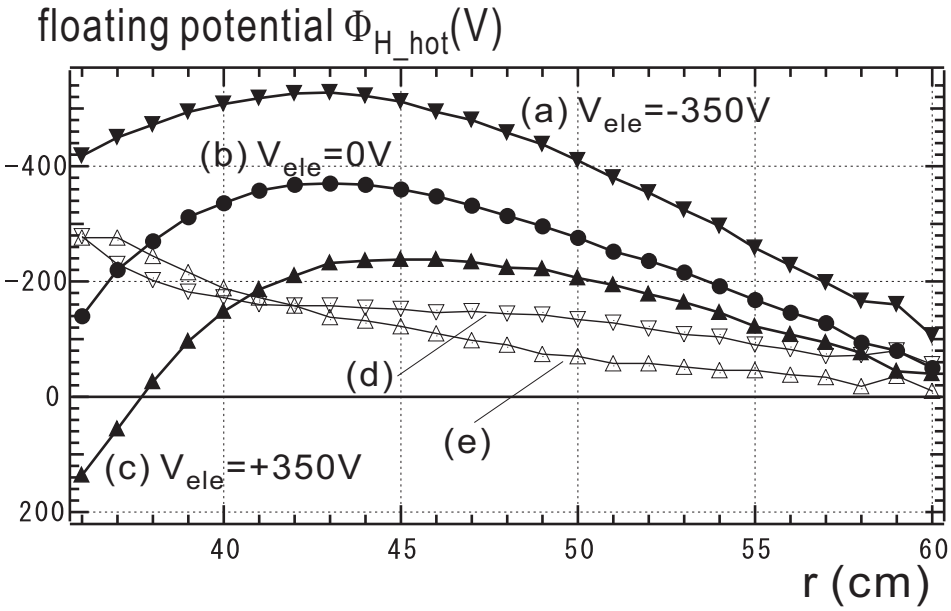

Figure 4.16: Potential control by the IC electrode. Profiles at $z = 0$ *cm*. Dipole configuration, and electrons were injected by the acceleration voltage of $V_acc = 500\,V$. The IC electrode is located at $r = 30$ *cm*. The potential of the IC electrode V_{ele} (against the chamber) was (a): $-350\,V$, (b): $0\,V$, and (c): $+350\,V$. The differences between two profiles are also shown. (d): the difference between the curve (a) and (b). (d): the difference between the curve (b) and (c). profiles at $z = 0$ *cm*.

The profiles (d) and (e) of Fig. 4.17 show the alteration of the potential profiles due to the influence of the IC electrode. They are apparently similar to the curves of the vacuum potential, generated by the image charges induced on the IC electrode. However, when the electrode was negatively biased, the tail of the profile (d) does not drop rapidly. It implies that the distribution of the electrons also changed, due to the external fields.

The potential profiles inside of the IC electrode is shown in Fig. 4.17. As discussed in the previous subsection, the profile has separated two peaks, because the potential structure is surrounding the IC electrode. When the electrodes were biased, these profiles were changed according to the applied potentials, and consequently the electric fields were modified. The alteration of the potential profiles by the electrode's bias is given in Fig. 4.18.

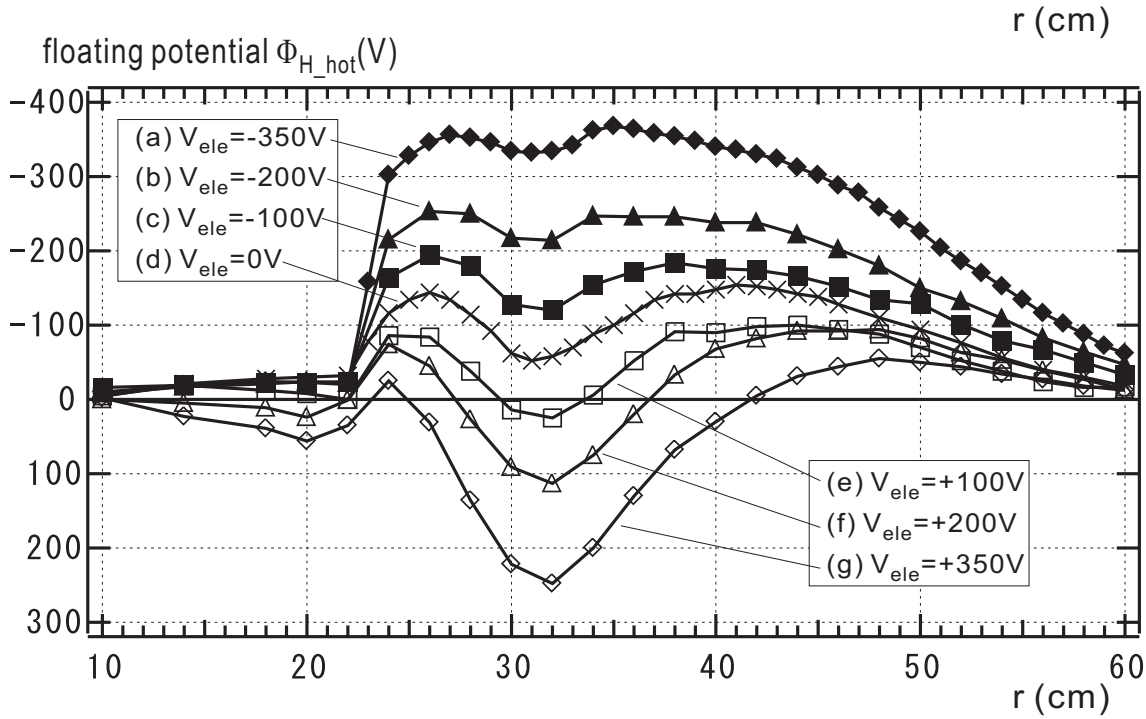

Figure 4.17: Potential control by the IC electrode. Profiles at $z = 8$ *cm*. Dipole configuration, $V_{acc} = 500$ *V*. The applied potential on the IC electrode V_{ele} was (a): -350 *V*, (b): -200 *V*, (c): -100 *V*, (d): 0 *V*, (e): $+100$ *V*, (f): $+200$ *V*, and (g): $+350$ *V*.

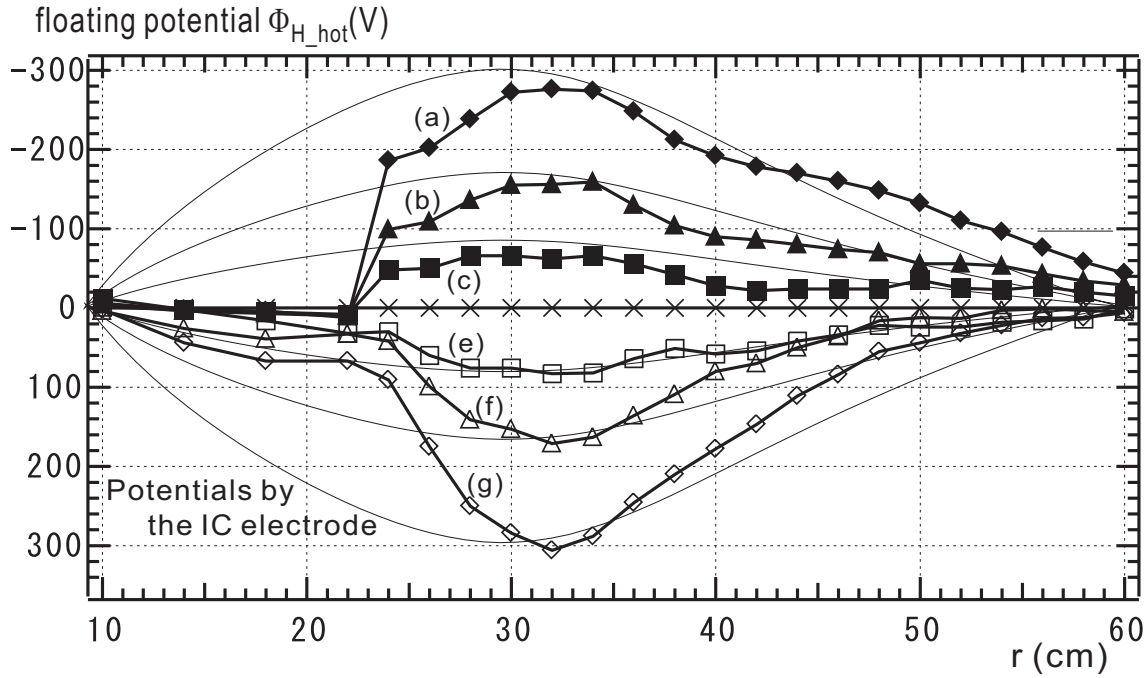

Figure 4.18: The differences between the profiles when $V_{ele} \neq 0$ and when $V_{ele} = 0$. The potential profile generated by the IC electrode of each potential are also shown.

Chapter 5

Summary

The equilibrium of a toroidal non-neutral plasma was numerically analyzed in a scope of the $\mathbf{E} \times \mathbf{B}$ drift model. The plasma shows paramagnetism being confined to the strong magnetic field side of the torus. The equilibrium is also controlled by externally applied electric fields, as well as by the magnetic field configurations. The effect of the external electric fields on the equilibrium is studied, and accordingly, new control method of a toroidal non-neutral plasma is discussed.

In contrast to liner traps, the electrostatic potential in the toroidal device is reduced by the image charges on conductive vessel or electrodes. The repression effect is quite large in toroidal-internal conductor devices, and it might contribute to the confinement of the particle.

The validity of the measurements by emissive probes was discussed and tested in the experiments. Because of the space charge limit, the floating potential V_f never agree with the space potential V_s of the plasma. However, the potential Φ_H measured by the high impedance-emissive probe can be regarded as an approximate value of the space potential, especially when the shapes of the plasma (rather than the value of the plasma) are measured. When the probe was directly hit by the electron beam, the drop of Φ_H by the emission is quite large, due to the long tail of the probe characteristics. It implies that the use of cold (non emissive) high impedance potential probe in the beam experiments is quite misleading.

The potential structures of a toroidal non-neutral plasma were measured in Proto-RT. The electrons were confined in the closed magnetic surface, surrounding the internal conductor coil. After the injection, the electrons were supposed to have diffused from the original beam orbit and the bulk component was formed. The shift toward the strong magnetic field region (”paramagnetism”) and toward the major axis of the torus was observed. However, the shape of the potential profiles does not agree with the numerical calculations from equilibrium model. It is due to the particle loss toward the vessel wall, perturbation by the support rods, the effects of beam component of the plasma, and the localized position of the particle source.

Aiming for an active control of a plasma, a pair of plasma control electrodes were installed in Proto-RT. The external electric fields generated by the electrodes penetrated into the plasma, and the alteration of the potential profile was observed. This method might be able to be applied for the improvement of the plasma property.

Appendix A

Electric circuits

A.1 Optional emissive probe circuit

In the measurements of emissive probes, the probe filament has a potential gradient due to the heating current, and it may cause perturbation to the plasma. To avoid this adverse effect, in the experiments of neutral plasmas, the half wave rectification power source is often employed for the filament heating, together with the sample and hold circuit.

In the experiments of non-neutral plasmas, however, the perturbation by the potential gradient in the probe tip is supposed to be quite small. In this study, the resistance of the probe filament was only $R \simeq 0.3\ \Omega$. Even when the probe is heated by its maximum current of $3\ A$, the voltage drop at the filament is less than $1\ V$. As compared with the typical space potential of the electron plasma in Proto-RT $V_S \simeq 1kV$, one can see that the perturbation by the potential gradient is not worth considering about. Rather, the generation of the electrons by the probe filament is possibly more serious.

The setup and the assembled electric circuit for the sample and hold measurements are shown for the future work. The schematic diagram is given in Fig. A.1, and the circuit is in Fig. A.2.

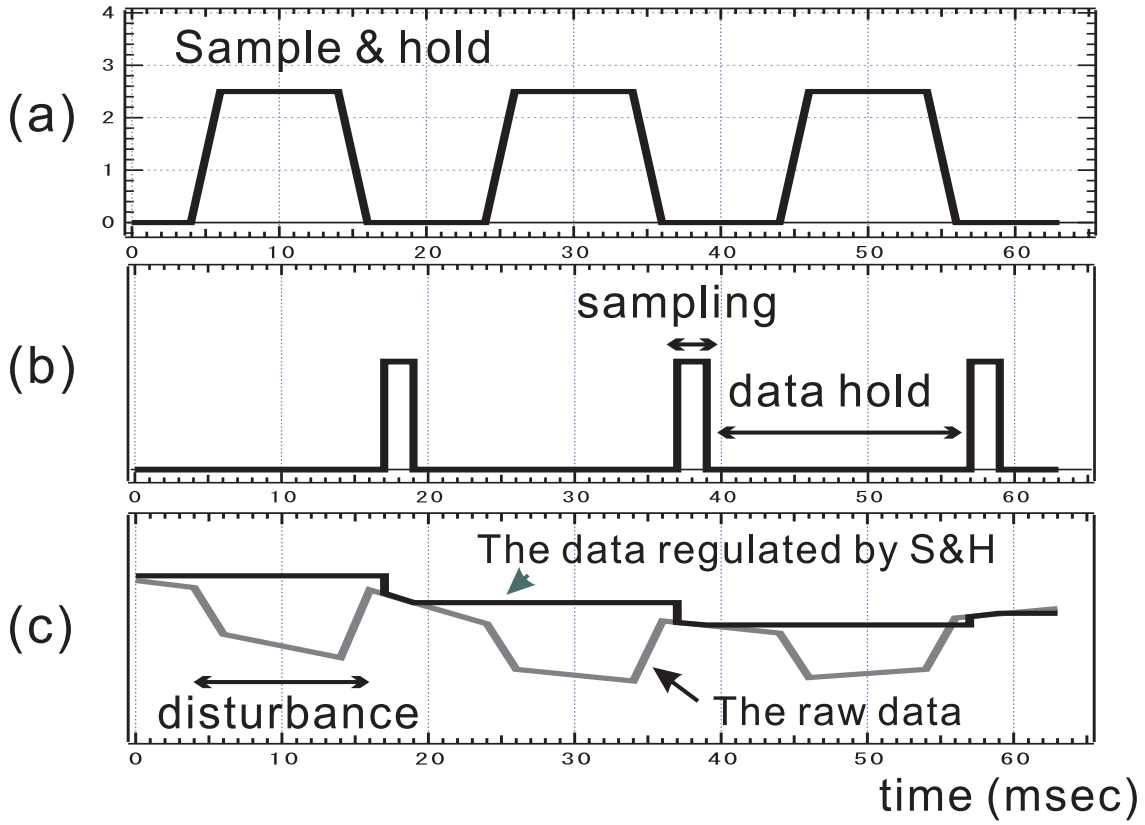

Figure A.1: The sample and hold circuit for emissive probes. Used for the purpose of reducing the perturbation due to the heating power source. (a) The output of the half wave rectificated power source. (b) The logic signal to the sample hold circuit. (c) The original raw data (there are perturbations during the heating.) and the data regulated by the sample and hold circuit.

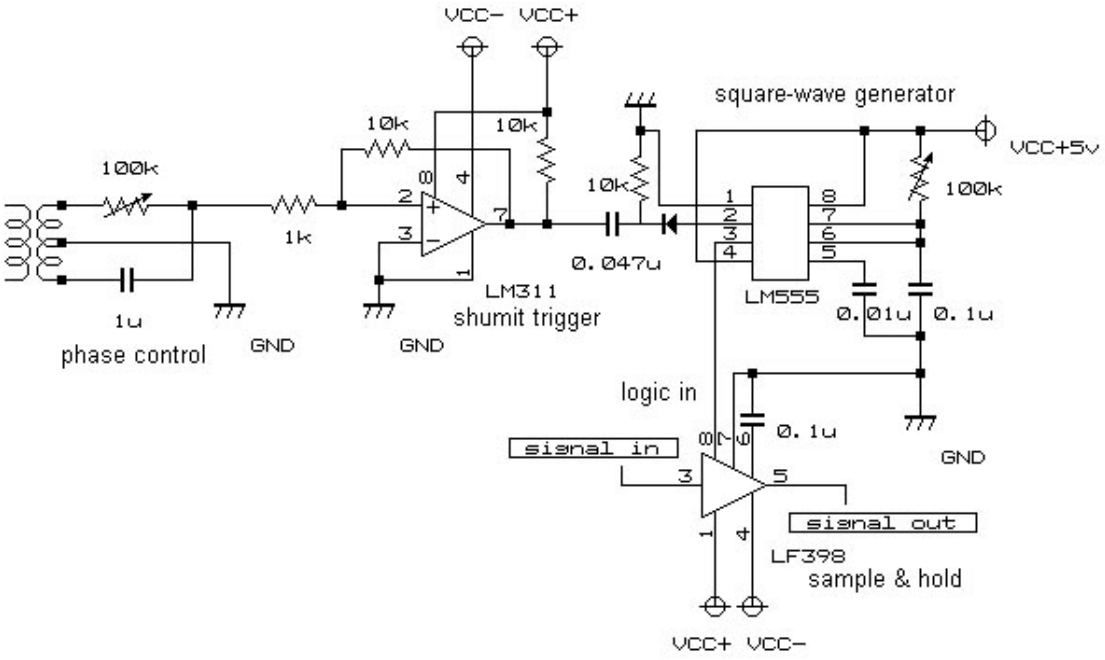

Figure A.2: The sample and hold circuit for emissive probes for the reduction of the influence of the potential disturbance due to the heating power source.

Bibliography

[1] C. M. Surko, M. Leventhal, and A. Passner: ”Positron Plasma in the Laboratory”, Phys. Rev. Lett. **62**, 901 (1989).

[2] S. M. Mahajan, Z. Yoshida: ”Double Curl Beltrami Flow: Diamagnetic Structures”, Phys. Rev. Lett. **81**, 4863 (1998).

[3] Z. Yoshida, S. M. Mahajan, S. Ohsaki, M. Iqbal, and N. Shatashvili: ”Beltrami Fields in Plasmas: High-Confinement Mode Boundary Layers and High Beta Equilibria”, Phys. Plasmas **8**, 2125(2001).

[4] J. D. Daugherty and R. H. Levy: ”Equilibrium of Electron Clouds in Toroidal Magnetic Fields”, Phys. Fluids **10** (1), 155 (1967).

[5] J. D. Daugherty, J. E. Eninger, G. S. Janes: ”Experiments on the Injection and Containment of Electron Clouds in a Toroidal Apparatus”, Phys. Fluids **12** (12), 2677 (1969).

[6] G. S. Janes: ”Experiments on Magnetically Produced and Confined Electron Clouds”, Phys. Rev. Lett. **15**, 135 (1965).

[7] P. Zaveri, P. I. John, K. Avinash, and P. K. Kaw: ”Low-Aspect-Ratio Toroidal Equilibria of Electron Clouds”, Phys. Rev. Lett. **68**, 3295 (1992).

[8] S. S. Khirwadkar, P. I. John, K. Avinash, A. K. Agarwal, and P. K. Kaw: ”Steady State Formation of a Toroidal Electron Cloud”, Phys. Rev. Lett. **71**, 4334 (1993).

[9] Z. Yoshida et al., H. Himura et al., C. Nakashima et al., *Nonneutral Plasma Physics III*, American Institute of Physics, 397-416 (1999).

[10] S. Kondoh:”Application of Magnetic Separatrix for a Charged-Particle Trap Using an Internal Conductor”, master’s thesis, department of quantum engineering and sistem sciences, The university of Tokyo (1997).

[11] S. Kondoh, Z. Yoshida: ”Toroidal Magnetic Confinement of Non-neutral Plasma”, Nucl. Inst. and Meth. in Phys. Res. A **382**, 561 (1996).

[12] C. Nakashima, Z. Yoshida: ”Application of RF Electric Field to a Charged-Particle Trap in Toroidal Geometry”, Nucl. Inst. and Meth. in Phys. Res. A **428**, 284 (1998).

[13] S. Kondoh, T. Tatsuno, Z. Yoshida ”Stabilization effect of magnetic shear on the diocotron instability”, Phys. Plasmas **8**, 2635 (2001).

[14] H. Saitoh, Z. Yoshida, C.Nakashima: ”Equilibrium of a Non-neutral Plasma in a Toroidal Magnetic Shear Configuration”, Rev. Sci. Instrum. 73, 87 (2002).

[15] K. Avinash: ”On Toroidal Equilibrium of Non-neutral Plasma”, Phys. Fluids B **3** (12), 3226 (1991).

[16] Ronald C. Davidson: *Physics of Nonneutral Plasma*, Assison-Weley Publishing company (1990).

[17] Leaf Turner: ”Brillouin Limit for Non-neutral Plasma in Inhomogeneous Magnetic Fields”, Phys. Fluids B **3**, 1355 (1991).

[18] Leaf Turner, D.C. Barns: ”Brillouin Limit and Beyond: A Route to Inertial-Electostatic Confinement of a Single-species Plasma”, Phys. Rev. Lett. **70**, 798 (1993).

[19] K. Ura et. al: *Electron Ion Beam Handbook*, Nikkan Kogyo Shinbun Ltd.(1998).

[20] Irving Langmuir: ”Electrical Discharges in Gases”, Rev. Modern Phys. **3**, 191 (1931).

[21] Francis F. Chen: ”Electric Probe”, in *Plasma Diagnostic Technique*, Academic Press Inc. (1991).

[22] Noah Hershkowitz: ”How Langmuir Probe Work”, in *Plasma Diagnostics*, Academic Press Inc. (1989).

[23] Robert F. Kemp, J. M. Sellen, Jr.: ”Plasma Potential Measured by Electron Emissive Probes”, in *Plasma Diagnostics*, Academic Press Inc. (1989).

[24] H. Himura, C. Nakashima, H. Saito, Z. yoshida: ”Probing of Flowing Electron Plasma”, Phys. Plasmas **8**, 4651 (2001).